The Astrophysical Journal, 979:130 (26pp), 2025 February 1 https://doi.org/10.3847/1538-4357/ad9c72

Chandra Follow-up Observations of Swift-BAT-selected AGNs III

Isaiah S. Cox[1,7], Núria Torres-Albà[1], Stefano Marchesi[1,2,3], Peter Boorman[4], Xiurui Zhao[5], Ross Silver[6], Marco Ajello[1], and Indrani Pal[1]
[1] Department of Physics and Astronomy, Clemson University, Clemson, SC 29634, USA
[2] Dipartimento di Fisica e Astronomia, Università degli Studi di Bologna, via Gobetti 93/2, 40129 Bologna, Italy
[3] INAF—Osservatorio Astronomico di Bologna, Via Piero Gobetti, 93/3, I-40129 Bologna, Italy
[4] Cahill Center for Astronomy and Astrophysics, California Institute of Technology, Pasadena, CA 91125, USA
[5] Department of Astronomy, University of Illinois at Urbana-Champaign, Urbana, IL 61801, USA
[6] NASA-Goddard Space Flight Center, Code 660, Greenbelt, MD 20771, USA
Received 2024 September 13; revised 2024 December 6; accepted 2024 December 7; published 2025 January 22

Abstract

The cosmic X-ray background (CXB) is dominated by the obscured and unobscured coronal light of active galactic nuclei (AGN). At energies below 10 keV, the CXB can be well explained by models taking into account the known AGN and the observed distribution of their obscuring, line-of-sight column densities, $N_{\rm H,l.o.s}$. However, at energies around the Compton reflection hump (~30 keV), the models fall short of the data. This suggests the existence of a population of as yet undetected Compton-thick (CT) AGN ($N_{\rm H,l.o.s} > 1.5 \times 10^{24}$ cm^{-2}) whose X-ray spectra are dominated by the light that has been reprocessed by the obscuring material. In this work, we continue the effort to find and catalog all local ($z < 0.05$) CT AGN. To this end, we obtained soft X-ray data with Chandra for six local BAT detected sources lacking ROSAT (0.1–2.4 keV) counterparts, indicating potential obscuration. We fit their spectra with Bayesian and least squares methods using two different models, `borus02` and `UXCLUMPY`. We compare the results of the different models and methods and find that the $N_{\rm H,l.o.s}$ is consistently measured in each case. Three of the sources were also observed with XMM-Newton, allowing the opportunity to search for variability in soft X-ray flux or $N_{\rm H,l.o.s}$. From this sample, we find one strong CT candidate (NGC 5759) and one weaker CT candidate (CGCG 1822.3+2053). Furthermore, we find tentative evidence of $N_{\rm H,l.o.s}$ variability in 2MASX J17253053–4510279, which has $N_{\rm H,l.o.s} < 10^{22}$ cm^{-2}.

Unified Astronomy Thesaurus concepts: Active galactic nuclei (16); X-ray active galactic nuclei (2035); Seyfert galaxies (1447); X-ray astronomy (1810)

1. Introduction

With the advent of high-sensitivity, imaging soft X-ray telescopes such as Chandra and XMM-Newton, it is now well-established that active galactic nuclei (AGN) are the main contributors to the cosmic X-ray background (CXB, e.g., D. M. Alexander et al. 2003; P. Gandhi & A. C. Fabian 2003; R. Gilli et al. 2007; E. Treister et al. 2009; Y. Ueda et al. 2014; N. Cappelluti et al. 2017; T. T. Ananna et al. 2019). The accretion of matter onto the central supermassive black hole in these objects results in UV and optical photons being upscattered to X-ray energies by the high energetic plasma in the corona, producing a power law with a photon index ~1.6–2.0 (e.g., F. Haardt & L. Maraschi 1993; K. Nandra & K. A. Pounds 1994; J. N. Reeves & M. J. L. Turner 2000). In most sources, this power law is attenuated by intervening matter through photoelectric absorption, which causes a change in the spectral shape, as lower energy X-rays are preferentially absorbed. The strength of this effect depends on the amount of intervening matter which is parameterized by the hydrogen column density in the line of sight, $N_{\rm H,l.o.s}$. Therefore, the shape of the CXB depends on the distribution of $N_{\rm H,l.o.s}$ in the AGN population (e.g., G. Ghisellini et al. 1994; G. Matt & A. C. Fabian 1994; A. Comastri et al. 1995; R. Gilli et al. 1999).

Models accounting for the distribution of $N_{\rm H,l.o.s}$ in the AGN population are able to reproduce the CXB emission below 10 keV (e.g., M. A. Worsley et al. 2005; R. C. Hickox & M. Markevitch 2006). However, the excess in the CXB data at higher energies around the Compton hump (~30 keV) indicates the presence of a population of Compton-thick (CT) AGN with very strong absorption ($N_{\rm H,l.o.s} > \sigma_T^{-1} \sim 10^{24}$ cm^{-2}; M. Ajello et al. 2008). At these energies, <40% of the CXB has been resolved by NuSTAR (e.g., F. A. Harrison et al. 2016). Models indicate that the CT fraction in the local universe could be up to 30%–50% (e.g., R. Gilli et al. 2007; Y. Ueda et al. 2014; T. T. Ananna et al. 2019). Hard X-ray, flux limited observations so far have shown that this fraction is only < 20% (e.g., R. Della Ceca et al. 2008; D. Burlon et al. 2011; R. V. Vasudevan et al. 2013; C. Ricci et al. 2015; G. Lanzuisi et al. 2018; N. Torres-Albà et al. 2021). There are currently only 66 AGN[8] that have NuSTAR observations confirming their CT nature (P. G. Boorman et al. 2024). It is important to find and catalog all of the CT-AGN within a volume-limited ($z < 0.05$), complete sample to estimate the true CT fraction and confirm their contribution to the CXB.

Furthermore, the radiation from these objects is typically dominated by the reflection component coming from reprocessing of the primary power law by the surrounding material. This region is commonly referred to as the dusty torus. It is

[7] Corresponding author.

[8] All 66 sources have $z < 0.1$. At $z \gtrsim 0.05$, only quasars with $L_{2-10\ \rm keV} > 10^{44}$ erg s^{-1} have been found to be CT.

often used to explain infrared observations as well as the observed differences between many classes of AGN (e.g., R. Antonucci 1993; C. M. Urry & P. Padovani 1995). The X-ray signature of the torus is usually drowned out by the primary power law originating from the corona. However, in CT-AGN, the absorption at energies >10 keV is strong enough to allow the reflection component to outshine the primary power law and be detected by NuSTAR (e.g., P. Arévalo et al. 2014; F. E. Bauer et al. 2015).

Physically motivated torus models such as MYTorus (K. D. Murphy & T. Yaqoob 2009), borus02 (M. Balokovic et al. 2018) and UXCLUMPY (J. Buchner et al. 2019) can be used to model the X-ray spectra of CT-AGN and constrain properties of the torus geometry (e.g., S. Marchesi et al. 2019; X. Zhao et al. 2021). However, the small number of known CT-AGN limits the conclusions we can make about the torus and different models can sometimes yield conflicting results on the torus parameters, such as the covering factor (e.g., M. Brightman et al. 2015; T. Saha et al. 2022; P. G. Boorman et al. 2024; K. Kallová et al. 2024). By increasing the number of known CT-AGN, we can further understand the nature of the obscuring material in AGN as well as the AGNs' contribution to the CXB.

Combining data from both hard X-ray telescopes such as Swift-BAT (S. D. Barthelmy et al. 2005) along with soft X-ray data from Chandra and/or XMM-Newton, for example, has been shown to be a reliable method for selecting candidate CT-AGN. S. Marchesi et al. (2017a) and R. Silver et al. (2022a) used a program to identify hard X-ray sources from the 150-month Swift-BAT catalog and observe them with quick (~10 ks) Chandra exposures resulting in ~95% of sources being obscured and ~20% being CT candidates (R. Silver et al. 2022a). The simultaneous fitting of the Chandra and Swift-BAT data provides an estimate of $N_{\rm H,l.o.s}$ which can be confirmed with a follow-up NuSTAR observation (e.g., S. Marchesi et al. 2017b, 2018; X. Zhao et al. 2019a, 2019b; N. Torres-Albà et al. 2021; A. Traina et al. 2021; R. Silver et al. 2022b; D. Sengupta et al. 2023). By this method, the population of known CT-AGN can be slowly increased and their tori properties can be constrained.

In this work, we continue the effort of the Clemson-INAF CT AGN project (CI-CTAGN)[9] which has so far confirmed ~30 CT-AGN in the local universe. We present the first Chandra results of six AGN selected according to the method explained in R. Silver et al. (2022a) and outlined below. We fit these Chandra data simultaneously with the Swift-BAT and XMM-Newton data (when available) to provide 1–150 keV coverage to constrain the line-of-sight $N_{\rm H,l.o.s}$ and torus geometrical properties. For those sources with XMM-Newton and Chandra data available, we also look for evidence of variability in $N_{\rm H,l.o.s}$, as has been done in recent works (e.g., A. Pizzetti et al. 2022; N. Torres-Albà et al. 2023; A. Pizzetti et al. 2025).

In Section 2, we briefly recount the selection criteria from R. Silver et al. (2022a) and present the data and reduction methods. In Section 3, we present the fitting methods and models used to obtain the $N_{\rm H,l.o.s}$ and torus parameters. We present the results of the modeling and provide CT-AGN candidates in Section 4. In Section 5, we compare the results of the models and fitting methods and discuss potential variability in obscuration. We summarize our results and discuss future work in Section 6.

We adopt a cosmology with $H_0 = 70\,{\rm km\,s^{-1}\,Mpc^{-1}}$, $\Omega_m = 0.27$, and $\Omega_\Lambda = 0.73$. All reported errors are at a 90% confidence level unless otherwise stated.

2. Sample Selection and Data

The sample in this work was selected from hard X-ray sources detected by Swift-BAT (in 15–150 keV) that lack a ROSAT (W. Voges et al. 1999) counterpart (in 0.1–2.4 keV). Five of the sources are from the 150-month Swift-BAT catalog (K. Imam et al. 2024, in preparation[10]), while one source (2MASX J17253053–4510279) is from the 157-month Swift-BAT catalog (A. Lien et al. 2024, in preparation[11]) while also being detected in the 105 month catalog (K. Oh et al. 2018). The five sources from the 150-month Swift-BAT catalog were processed by the BAT_IMAGER code (A. Segreto et al. 2010) and their spectra have been background subtracted and averaged over the entire 150 month exposure time.

The fact that these sources were detected in hard X-rays but not soft X-rays indicates possible X-ray obscuration with column densities $N_{\rm H,l.o.s} > 10^{23}\,{\rm cm^{-2}}$ (see e.g., M. Ajello et al. 2008, and M. J. Koss et al. 2016). However, R. Silver et al. (2022a) showed that this threshold may be lower ($N_{\rm H,l.o.s} \gtrsim 5 \times 10^{22}\,{\rm cm^{-2}}$) as the 150-month Swift-BAT catalog goes deeper in flux and detects intrinsically fainter sources. Furthermore, we avoided sources classified as Seyfert 1 because the presence of strong broad lines in the optical spectrum is generally correlated with unobscured AGN (e.g., M. Koss et al. 2017). Among our sources, only MCG +02-57-2 is classified as a Seyfert 1.9, indicating only a weak Hα broad line present (K. L. Smith et al. 2020), and some Seyfert 1.9 galaxies have large $N_{\rm H,l.o.s}$ values (e.g., T. T. Shimizu et al. 2018). We note that while Seyfert 2 galaxies are more obscured than Seyfert 1 s on average (see e.g., S. Marchesi et al. 2016), a significant fraction (as high as 66%, e.g., O. Garcet et al. 2007) of Seyfert 2 galaxies are found to have unobscured X-ray emission in some samples. It should also be noted that although we exclude Seyfert 1 galaxies from our selection, they can also be obscured in the X-rays (e.g., G. Risaliti et al. 2001, 2007; A. Merloni et al. 2014; G. Miniutti et al. 2014; T. T. Shimizu et al. 2018; R. Serafinelli et al. 2023).

2.1. Chandra

All six objects in our sample were observed with ACIS-S for ~10 ks during Chandra guest observing Cycle 23 (ID: 23700077, P.I. Silver.[12]). The observations can be downloaded at DOI: 10.25574/cdc.321. A summary of the sample along with the Chandra observation date and 1–7 keV count rate is shown in Table 1. The Chandra data were reduced and spectra were obtained by following standard procedures using the CIAO version 4.13 software (A. Fruscione et al. 2006). We used a 5″ circular region for the source and an annulus with $r_{\rm in} = 6''$ and $r_{\rm out} = 15''$ for the background region. We used CIAO specextract to extract the spectrum in each of these regions. We then binned the source spectrum to 5 counts bin^{-1}

[9] https://science.clemson.edu/ctagn/

[10] The 150 month catalog can be found here https://science.clemson.edu/ctagn/bat-150-month-catalog/.

[11] The 157 month catalog can be found here https://swift.gsfc.nasa.gov/results/bs157mon/.

[12] https://cxc.harvard.edu/cgi-bin/propsearch/prop_details.cgi?pid=6115

Table 1
Summary of the Sample and the Related X-Ray Observations

Source Name	R.A. (J2000)	Decl. (J2000)	Redshift	Counts (Rate)[a] Chandra	Counts (Rate)[b] XMM-Newton	Obsid Chandra	Obsid XMM-Newton
2MFGC 9836	187.206082	−29.627365	0.0276	788 (7.91E-2)	⋯	25258	⋯
NGC 5759	221.811739	13.456590	0.0277	36 (3.36E-3)	288 (1.43E-2)	25257	0881840201
IC 1141	237.445689	12.399175	0.0147	80 (7.92E-2)	⋯	25256	0881840101[c]
2MASX J17253053–4510279	261.377141	−45.174592	0.0196	683 (6.85E-2)	1846 (7.84E-1)	25260	0881840501
CGCG 1822.3+2053	276.110536	20.902621	0.0167	67 (6.61E-3)	547 (6.95E-2)	25259	0881840401
MCG +02-57-2	335.937290	11.835737	0.0294	1514 (1.52E-1)	⋯	25261	⋯

Notes. All Chandra observations are 10 ks long.
[a] These are the total counts (count rate) used in the fitted spectrum.
[b] These are the sum of the total counts (count rates) used in the fitted spectra from both MOS cameras and the PN camera.
[c] These data are not used due to strong background flaring throughout the exposure.

for spectral fitting with the W statistic, cstat (K. Wachter et al. 1979).

2.2. XMM-Newton

Three of the sources in our sample also have available data from XMM-Newton (CGCG 1822.3+2053, 2MASX J17253053–4510279, and NGC 5759) (ID: 088184, P.I. Silver, European Space Agency 2023). The cleaned exposure times for CGCG 1822.3+2053 are 8.1 ks, 8.0 ks, and 5.3 ks for the MOS-1, MOS-2, and PN cameras, respectively. For 2MASX J17253053–4510279, the cleaned times are 4.1 ks, 3.9 ks, and 1.1 ks, and for NGC 5759 the cleaned times are 13.7 ks, 13.5 ks, and 9.7 ks. The XMM-Newton data were reduced following standard procedures using the SAS version 21.0.0 (F. Jansen et al. 2001). To extract the spectra, we used a 30″ circular region for the source and a 45″ circular region for the background. The background region was chosen as close as possible to the source and at a similar height on the CCD while avoiding contamination from other sources. The spectra were binned to 5 counts bin^{-1} for fitting with cstat. The Chandra and XMM-Newton images of CGCG 1822.3+2053 with the source and background extraction regions are shown in Figure 1, as an example.

3. Spectral Analysis

We simultaneously fit the Chandra, Swift-BAT, and XMM-Newton (when available) data using two different regression methods and two different torus models. Simultaneously fitting the soft X-ray data from Chandra and XMM-Newton with the hard X-ray data from Swift-BAT is useful to break the degeneracy between the photon index and the $N_{\rm H,l.o.s}$ in obscured sources. For consistency with the analysis in R. Silver et al. (2022a), we exclude data below 1 keV because it contains little information on $N_{\rm H,los}$ for moderately to heavily obscured sources. Excluding these data allow for simpler models while still providing accurate constraints on $N_{\rm H,los}$. Furthermore, the `borus02` model is tabulated only for energies >1 keV and we decide to keep the fitted energy range consistent across all models. We describe the regression methods and models in this section.

3.1. Regression Methods

We use two different regression algorithms to perform the fits. We describe them in this section.

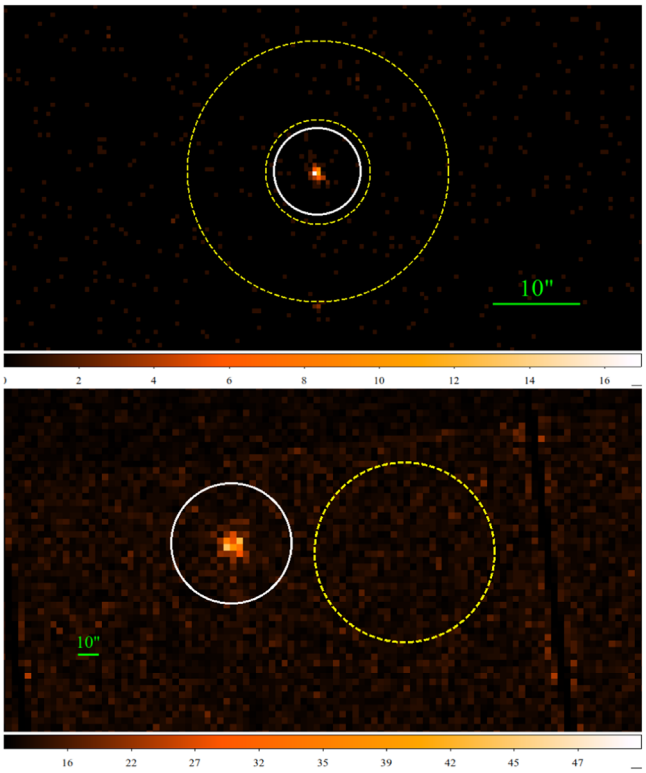

Figure 1. Top panel: Image showing the Chandra data for CGCG 1822.3+2053 with the source extraction region indicated by the solid white circle and the background extraction region indicated by the dashed yellow annulus. Bottom panel: Source and background extraction regions for the XMM-Newton data overlayed on an image from the EPIC-PN camera. In both panels, north is up and east is left.

3.1.1. Levenberg–Marquardt

Most commonly, X-ray spectra are fitted using some variation of the least squares method. The computational requirements of this method are relatively light; however, the regression can lead to local minima rather than the global minimum. Therefore, the results are potentially sensitive to the initial parameter values. Furthermore, linear approximations are required, which can significantly affect results when the model exhibits nonlinearity. Nevertheless, this type of regression is most commonly used in X-ray spectral fitting due to the computational efficiency.

The final results of this type of fitting are an estimate on the value of parameters of interest along with confidence intervals

Table 2
Summary of Initial Inputs and Priors

Model	borus02	UXCLUMPY	borus02	UXCLUMPY
	Least Squares Initial Input		Bayesian Prior	
Γ	1.8	1.8	Uniform(1.4,2.6)	Uniform(1.4,2.6)
$\log(N_{\rm H,tor}/{\rm cm}^{-2})$	24	⋯	Uniform(22,25.5)	⋯
$CF_{\rm tor}$	0.67	⋯	Uniform(0.1,1.0)	⋯
$\theta_{\rm inc}(^\circ)$	45	90	Uniform(19,87)	Uniform(0,90)
$\sigma_{\rm tor}$	⋯	28	⋯	Uniform(6,84)
CTKcover	⋯	0	⋯	Uniform(0.0,0.6)
$N_{\rm H}(10^{22}\ {\rm cm}^{-2})$	10	10	Uniform(0.1,500)	Uniform(0.1,500)

Note. The bounds for torus geometry parameters and photon index span the entire allowable range for each model.

for each parameter. The best parameter estimate is the value of the parameter resulting in the model with the smallest fit statistic that the regression was able to find. The confidence interval for parameters of interest can be calculated with the `steppar` command, which steps through a range of parameter values and computes the fit statistic with the parameter fixed at each step value. We take the 90% confidence interval to be the range of parameter values for which the difference between the fit statistic and the minimum fit statistic is less than 2.7 (e.g., M. Bonamente 2020).

We use the Levenberg–Marquardt (LM) algorithm built in to `XSPEC` version 12.11.1 for the least squares regression. We fit all data available for each source using the models outlined in Section 3.2. We begin each fit with the same set of parameters for each source. In particular, we start at $\Gamma = 1.8$ and $N_{\rm H}/(10^{22}\ {\rm cm}^{-2}) = 10$ with all the torus parameters frozen. We then thaw the torus geometry parameters one at a time and ensure that we reach a stable fit by running `error` calculations on each free parameter until no new best fits are found. The output of the `steppar` calculation is used to create confidence contours on $N_{\rm H}$ and Γ.

3.1.2. Nested Sampling

An alternative to the LM algorithm is to use a Bayesian approach, which we accomplish using nested sampling (J. Buchner 2023; J. Buchner & P. Boorman 2024). This method allows for a global search over complex parameter spaces, and therefore avoids getting trapped in local minima. The primary downside of nested sampling is the computation time. For models with more than a few free parameters and multiple observations, this method becomes infeasible without the use of high-performance computing clusters.

The final result of this Bayesian approach is the posterior distributions for each parameter of interest. The posterior distribution contains all of the information obtainable about the unknown parameter from the prior knowledge of the parameter and the information in the observed data. We take the best estimate of the parameter to be the most probable value of the posterior distribution. We take the 90% confidence interval (or "credible" interval) to be the interval containing 90% of the posterior, with the mass below and above the interval being equal. That is, we calculate the 5th and 95th percentiles, and exclude the values outside this range.

To obtain the posterior distributions, we use the Bayesian X-ray analysis tool `BXA` (J. Buchner et al. 2014) version 4.0.5, which uses the nested sampling algorithm `UltraNest` (J. Buchner 2021) within the `PyXSPEC` (C. Gordon & K. Arnaud 2021) fitting environment. We use uniform priors for the photon index, $N_{\rm H,los}$ and torus geometry parameters, see Table 2. We use log-uniform priors (i.e., uniform priors on a log scale) for the normalization, cross-normalization, and scattering fraction parameters. The fits for each source were performed on Clemson University's high-performance computing cluster, Palmetto, using 20 cores and 16 GB RAM. With these specifications, the computation time required ranged from a few hours (for IC 1141) up to a few hundred hours (for CGCG 1822.3+2053).

3.2. Models

We use two different physically motivated torus models (`borus02` and `UXCLUMPY`) to model the reflection component seen in the X-ray spectrum. In most cases, the parameters determining the reflection component are unconstrained, so we also use simpler model configurations (`borus02`* and `MYTorus`) as a consistency check for the $N_{\rm H,los}$ results. A summary of the initial guesses and priors for parameters of interest is shown in Table 2.

3.2.1. borus02

The first model is `borus02` (M. Balokovic et al. 2018). This model assumes a uniform density, spherical torus with conical polar cutouts. The opening angle is determined by the covering factor $c_f = \cos(\theta_{\rm torus})$, which we leave free to vary in the range 0.1–1.0. The inclination angle with respect to the observer is provided as $\cos(\theta_{\rm inc})$ and is left free to vary between 0.05 (edge-on) and 0.95 (face-on). The torus column density, $\log(N_{\rm H,\,torus}/{\rm cm}^{-2})$, is left free to vary between 22.0 and 25.5. The model provides the relative abundance of iron as a parameter; however, we chose to leave it fixed at the solar abundance. This torus geometry is illuminated by an X-ray source located at the center, radiating with a photon index, Γ, and a high-energy cutoff, $E_{\rm cut}$. We leave Γ free to vary between 1.4 and 2.6. We leave $E_{\rm cut}$ fixed at 300 keV (Y. Ueda et al. 2014; M. Baloković et al. 2020) in all sources.

To account for the line-of-sight component, we add a primary power law (with parameters tied to the X-ray source in the torus component) attenuated by photoelectric absorption (*zphabs*) and Compton scattering out of the line of sight (*cabs*). We also add a scattering component which is parameterized as a fraction, f_s, of the primary power law to account for elastic scattering of X-rays into the line of sight.

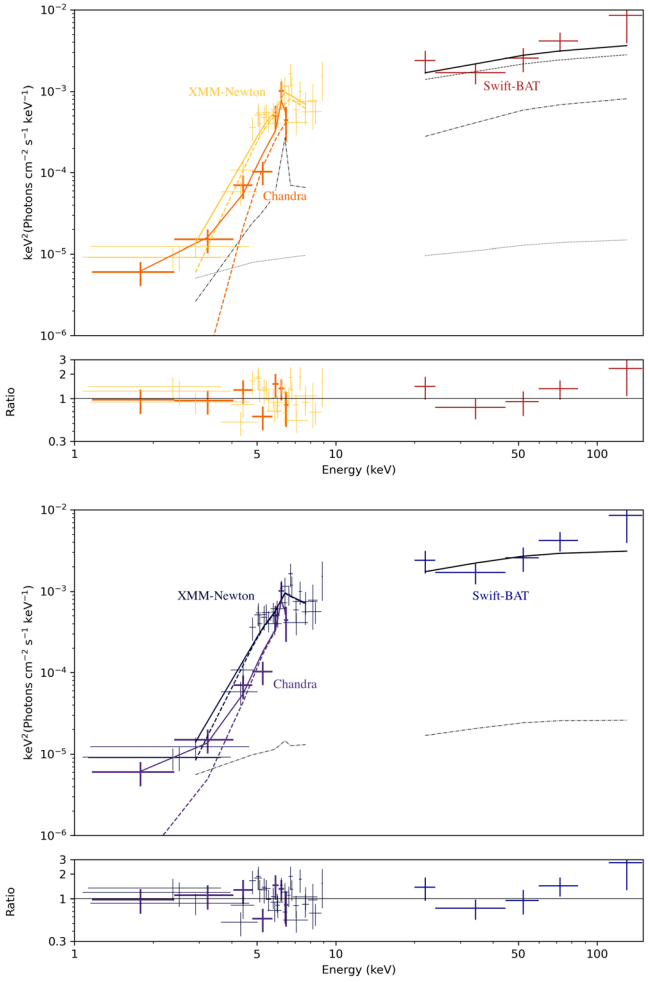

Figure 2. CGCG 1822.3+2053. Top panel: Best fit with the `borus02` model (solid lines). The binned Chandra (thick orange), XMM-Newton (thin yellow), and Swift-BAT (red) data are shown with the intrinsic (dashed lines), reflection (dashed–dotted lines), and scattering (dotted lines) components. Bottom panel: Best fit with the `UXCLUMPY` model (solid lines). The dashed lines show the transmitted and reflected components, while the dashed–dotted lines show the scattered component in `UXCLUMPY`.

The model is implemented in `XSPEC` as

$$\begin{aligned}\texttt{borus02} = C \cdot \textit{phabs} \cdot (&\text{borus02\_v170323a.fits} \\ &+ \textit{zphabs} \cdot \textit{cabs} \cdot \textit{zcutoffpl} \\ &+ f_s \cdot \textit{zcutoffpl}),\end{aligned}$$

where C is a constant to account for flux variability between observations and *phabs* accounts for Galactic absorption.

3.2.2. *UXCLUMPY*

The second model is `UXCLUMPY` (J. Buchner et al. 2019). This model accounts for the clumpiness of the torus and assumes a distribution of spherical clouds surrounding a central X-ray source producing a cutoff power law similar to `borus02`. We again leave the photon index free to vary between 1.4 and 2.6 and $E_{\rm cut}$ fixed at 300 keV.

The torus cloud geometry is determined by the parameter *TORsigma*, which sets the width of the Gaussian distributed cloud distribution. We leave this parameter free to vary between 6° and 84°. The inclination angle is left free to vary between 0° (face-on) and 90° (edge-on). To account for strong reflection in some sources, the parameter *CTKcover* provides an additional CT reflecting component with a covering factor that we leave free to vary between 0 and 0.6. Unlike `borus02`, the hydrogen column density, $N_{\rm H}$, provided by `UXCLUMPY` is the $N_{\rm H,l.o.s}$. Both photoelectric absorption and Compton scattering are accounted for in the model. We compare the best-fit value for this parameter to the value found for *zphabs* and *cabs* in `borus02`.

The scattering component is also computed by `UXCLUMPY` as a warm mirror which can scatter the primary power law as well as some reflected emission into the line of sight. These parameters are tied to the main parameters and the strength is set with the scattering fraction f_s similar to `borus02`.

The total model is implemented in `XSPEC` as

$$\begin{aligned}\texttt{UXCLUMPY} = C \cdot \textit{phabs} \cdot (&\text{uxclumpy-cutoff.fits} \\ &+ f_s \cdot \text{uxclumpy-cutoff-omni.fits}).\end{aligned}$$

3.2.3. *borus02**

In general, the data presented in this paper are not of high enough quality to constrain the AGN torus parameters. Therefore, we also fit each source using the `borus02` model with the parameters $N_{\rm H,tor}$, c_f, and $\cos(\theta_{\rm inc})$ frozen at their typical values, as reported in X. Zhao et al. (2021). In this work, the authors find that for both Compton-thin and CT-AGN, the average torus column density is $\log(N_{\rm H,tor}/\,{\rm cm}^{-2}) \sim 24$ and the average covering factor is ~0.67 for Compton-thin sources. Since the distribution of torus inclination angles should be uniform between 0° and 90°, we fix the value to 45° for lack of a better choice and to minimize the bias of assuming either an edge-on or a face-on scenario.

3.2.4. *MYTorus*

We also use the `MYTorus` (K. D. Murphy & T. Yaqoob 2009) model with $N_{\rm H,los}$ coupled to the $N_{\rm H,tor}$ for the sources with only one soft X-ray observation. The model assumes a true torus geometry with a fixed half-opening angle of 60°, which corresponds to a covering factor of 0.5. We leave the inclination angle fixed at 90° (edge on).

For the sources with two soft X-ray observations, we use the model with $N_{\rm H,los}$ decoupled from the $N_{\rm H,tor}$ to account for variability. We leave the inclination angle fixed at 90° for the `MYtorusZ` component which includes the line-of-sight absorption. The inclination angle for the `MYtorusS` and `MYtorusL` components is fixed at 45° and the $N_{\rm H,tor}$ is fixed at $1.0 \times 10^{24}\,{\rm cm}^{-2}$ to match the `borus02`* model.

The total model is implemented in `XSPEC` as

$$\begin{aligned}\texttt{MYTorus} = C \cdot \textit{phabs} \cdot (&\text{mytorus\_Ezero\_v00.fits} \cdot \textit{zpowerlw} \\ &+ C_S \cdot \text{mytorus\_scatteredH300\_v00.fits} \\ &+ C_L \cdot \text{mytl\_V000010nEp000H500\_v00.fits} \\ &+ f_s \cdot \textit{zpowerlw}).\end{aligned}$$

where $C_S = C_L = 1$. The $N_{\rm H}$ in the `MYtorusZ` component is allowed to vary between the Chandra and XMM-Newton observations where applicable, as it is in the other three models.

The `MYTorus` model as implemented is unable to fit unobscured sources with $N_{\rm H,los} < 10^{22}\,{\rm cm}^{-2}$. Our sample includes two sources (2MASX J17253053–4510279 and MCG +02-57-2) for which that is the case. Since the reflection

Table 3
Summary of $N_{\rm H,l.o.s}(10^{22}{\rm cm}^{-2})$ Measurements

Model	MYTorus	borus02*	borus02	UXCLUMPY	MYTorus	borus02*	borus02	UXCLUMPY
		Least Squares				Bayesian		
2MFGC 9836	$17.2^{+2.5}_{-2.3}$	$17.4^{+1.5}_{-2.7}$	$18.3^{+2.5}_{-3.0}$	$14.4^{+3.7}_{-1.5}$	$16.9^{+2.7}_{-2.0}$	$16.8^{+2.8}_{-2.0}$	$17.3^{+3.9}_{-2.1}$	$15.9^{+2.7}_{-2.5}$
NGC 5759 (Ch)	50^{+63}_{-24}	$36.1^{+43.8}_{-19.8}$	36^{+42}_{-16}	50^{+75}_{-29}	81^{+350}_{-30}	51.2^{+390}_{-22}	65^{+390}_{-27}	110^{+340}_{-48}
NGC 5759 (XMM)	>52	>49	>53	>49	140^{+330}_{-50}	117^{+360}_{-36}	290^{+190}_{-190}	170^{+310}_{-57}
IC 1141	44^{+15}_{-12}	$42.4^{+19.4}_{-14.6}$	43^{+69}_{-13}	47^{+23}_{-16}	45^{+14}_{-13}	$43.2^{+21.5}_{-12.5}$	49^{+120}_{-15}	50^{+92}_{-15}
2MASX J17253053–4510279 (Ch)	$0.38^{+0.21}_{-0.18}$	$0.50^{+0.18}_{-0.20}$	⋯	$0.51^{+0.17}_{-0.16}$	$0.53^{+0.17}_{-0.17}$	$0.54^{+0.21}_{-0.15}$	⋯	$0.46^{+0.16}_{-0.14}$
2MASX J17253053–4510279 (XMM)	<0.15	<0.18	⋯	<0.27	$0.11^{+0.09}_{-0.01}$	$0.12^{+0.12}_{-0.02}$	⋯	$0.11^{+0.08}_{-0.01}$
CGCG 1822.3+2053 (Ch)	76^{+58}_{-27}	$63.2^{+38.9}_{-21.2}$	87^{+35}_{-27}	77^{+48}_{-22}	87^{+220}_{-25}	77^{+360}_{-22}	87^{+300}_{-25}	96^{+100}_{-30}
CGCG 1822.3+2053 (XMM)	46^{+11}_{-10}	$38.7^{+9.5}_{-6.4}$	54^{+16}_{-11}	50^{+21}_{-12}	48^{+12}_{-8}	43^{+9}_{-7}	53^{+16}_{-8}	55^{+16}_{-11}
MCG +02-57-2	<0.43	<0.35	⋯	<0.29	$0.13^{+0.27}_{-0.02}$	$0.15^{+0.28}_{-0.03}$	⋯	$0.13^{+0.23}_{-0.02}$

Note. The MYTorus column shows the results using the simple absorbed power-law model for 2MASX J17253053–4510279 and MCG +02-57-2.

Table 4
CGCG 1822.3+2053 Best-fit Results

Model	MYTorus	borus02*	borus02	UXCLUMPY	MYTorus	borus02*	borus02	UXCLUMPY
Algorithm		LM				Nested Sampling		
red χ^2	1.13	1.22	1.13	1.14	1.13	1.26	1.16	1.17
χ^2/d.o.f.	122/108	132/108	119/105	120/105	122/108	136/108	122/105	123/105
Γ	$1.60^{+0.43}_{-u}$	$1.40^{+0.37}_{-u}$	$1.55^{+0.62}_{-u}$	$1.54^{+0.77}_{-u}$	$1.73^{+0.40}_{-0.29}$	$1.64^{+0.31}_{-0.19}$	$1.81^{+0.49}_{-0.35}$	$2.09^{+0.34}_{-0.58}$
$N_{\rm H,tor}(10^{22}\ {\rm cm}^{-2})$	100^{*}	100^{*}	3200^{+u}_{-u}	⋯	100^{*}	100^{*}	37^{+2300}_{-31}	⋯
$CF_{\rm tor}$	⋯	0.67^{*}	0.20^{+u}_{-u}	⋯	⋯	0.67^{*}	$0.15^{+0.74}_{-0.04}$	⋯
$\theta_{\rm inc}(^\circ)$	45^{*}	45^{*}	78^{+u}_{-u}	90^{+u}_{-u}	45^{*}	45^{*}	79^{+7}_{-42}	64^{+21}_{-59}
$\sigma_{\rm tor}$	⋯	⋯	⋯	18^{+63}_{-u}	⋯	⋯	⋯	14^{+64}_{-5}
CTKcover	⋯	⋯	⋯	0^{+u}_{-u}	⋯	⋯	⋯	$0.39^{+0.17}_{-0.36}$
norm(10^{-3})	$0.9^{+1.8}_{-0.5}$	$0.4^{+0.6}_{-0.1}$	$1.61^{+6.78}_{-1.01}$	$1.63^{+37.3}_{-1.05}$	$1.7^{+2.7}_{-1.0}$	$1.0^{+0.6}_{-0.5}$	$2.14^{+7.90}_{-1.22}$	$5.82^{+13.0}_{-4.41}$
$f_{\rm s}(10^{-3})$	$4.26^{+5.30}_{-3.08}$	$5.97^{+4.76}_{-4.95}$	$3.26^{+3.49}_{-2.25}$	⋯	$3.01^{+2.93}_{-2.88}$	$2.12^{+2.75}_{-2.10}$	$2.33^{+2.72}_{-2.25}$	⋯
$f_{\rm s,uxclumpy}(10^{-3})$	⋯	⋯	⋯	$7.67^{+u}_{-6.48}$	⋯	⋯	⋯	$7.72^{+21.1}_{-7.61}$
$C_{\rm xmm}$	$0.94^{+0.67}_{-0.37}$	$1.08^{+0.60}_{-0.26}$	$0.78^{+0.58}_{-0.36}$	$0.83^{+0.59}_{-0.50}$	$0.75^{+0.62}_{-0.28}$	$0.85^{+0.62}_{-0.24}$	$0.69^{+0.67}_{-0.26}$	$0.68^{+0.63}_{-0.33}$
$C_{\rm BAT}$	$0.74^{+0.92}_{-0.39}$	$0.69^{+0.80}_{-0.23}$	$0.50^{+0.91}_{-0.31}$	$0.47^{+1.01}_{-0.27}$	$0.82^{+1.02}_{-0.41}$	$1.05^{+1.07}_{-0.50}$	$0.77^{+2.13}_{-0.48}$	$0.69^{+0.96}_{-0.39}$
$N_{\rm H,cha}(10^{22}\ {\rm cm}^{-2})$	76^{+58}_{-27}	63^{+39}_{-21}	87^{+35}_{-27}	77^{+48}_{-22}	87^{+220}_{-25}	77^{+360}_{-22}	87^{+300}_{-25}	96^{+100}_{-30}
$N_{\rm H,xmm}(10^{22}\ {\rm cm}^{-2})$	46^{+11}_{-10}	39^{+10}_{-6}	54^{+16}_{-11}	50^{+21}_{-12}	48^{+12}_{-8}	43^{+9}_{-7}	53^{+16}_{-8}	55^{+16}_{-11}
$\log(L_{\rm 2\text{-}10\,keV,\,cha})$	$42.4^{+0.2}_{-0.3}$	$42.2^{+0.2}_{-0.3}$	$42.7^{+0.2}_{-0.2}$	$42.8^{+0.5}_{-0.4}$	$42.4^{+0.2}_{-0.2}$	$42.2^{+0.2}_{-0.3}$	$42.9^{+0.2}_{-0.3}$	$43.0^{+0.3}_{-0.4}$
$\log(L_{\rm 2\text{-}10\,keV,\,xmm})$	$42.45^{+0.05}_{-0.05}$	$42.2^{+0.05}_{-0.06}$	$42.70^{+0.04}_{-0.05}$	$42.7^{+0.5}_{-0.4}$	$42.40^{+0.05}_{-0.05}$	$42.3^{+0.05}_{-0.06}$	$42.83^{+0.05}_{-0.05}$	$42.9^{+0.3}_{-0.4}$
$\log(L_{\rm 15\text{-}150\,keV})$	$43.0^{+0.1}_{-0.2}$	$42.9^{+0.2}_{-0.2}$	$43.2^{+0.1}_{-0.2}$	$43.0^{+0.5}_{-0.7}$	$43.0^{+0.1}_{-0.2}$	$42.7^{+0.2}_{-0.2}$	$43.0^{+0.1}_{-0.1}$	$43.0^{+0.4}_{-0.5}$
$\log(F_{\rm 2\text{-}10\,keV,\,cha})$	$-12.28^{+0.09}_{-0.09}$	$-12.29^{+0.09}_{-0.09}$	$-12.24^{+0.09}_{-0.09}$	$-12.21^{+0.09}_{-0.09}$	$-12.28^{+0.09}_{-0.09}$	$-12.30^{+0.09}_{-0.09}$	$-12.30^{+0.09}_{-0.09}$	$-12.25^{+0.09}_{-0.09}$
$\log(F_{\rm 2\text{-}10\,keV,\,xmm})$	$-12.07^{+0.04}_{-0.04}$	$-12.08^{+0.04}_{-0.04}$	$-12.04^{+0.04}_{-0.04}$	$-12.04^{+0.04}_{-0.04}$	$-12.07^{+0.04}_{-0.04}$	$-12.09^{+0.04}_{-0.04}$	$-12.06^{+0.04}_{-0.04}$	$-12.05^{+0.04}_{-0.04}$
$\log(F_{\rm 15\text{-}150\,keV})$	$-11.01^{+0.09}_{-0.12}$	$-11.00^{+0.09}_{-0.12}$	$-11.02^{+0.09}_{-0.12}$	$-11.04^{+0.09}_{-0.12}$	$-11.01^{+0.10}_{-0.12}$	$-11.06^{+0.10}_{-0.13}$	$-11.08^{+0.10}_{-0.13}$	$-11.11^{+0.10}_{-0.13}$
$P_{\rm ch}$(CT)	⋯	⋯	⋯	⋯	16.9%	33.8%	18.3%	10.4%
$P_{\rm xmm}$(CT)	⋯	⋯	⋯	⋯	0.0%	0.0%	0.0%	0.0%

Note. A *u* in the upper or lower limit indicates that the parameter is unconstrained in that particular direction. A * indicates that the parameter was frozen at that particular value during the fit. The luminosities shown are the intrinsic luminosities while the fluxes are observed.

component is not important for these two sources, we use a simple absorbed power law implemented in `XSPEC` as

$$\text{Simple} = C \cdot phabs \cdot zphabs \cdot zcutoffpl$$

in place of `MYTorus`.

4. Results

In this section, we present the fitting results for each individual source and discuss exceptions to the analysis presented in Section 3. Table 3 shows a summary of the measured $N_{\rm H,l.o.s}$ values for each source. Note that the χ^2 fit statistics shown in Tables 4–8 for the Bayesian method are computed using the parameters from the posterior that result in the maximum likelihood. In general, these values are not the same as the most probable value for the parameter, which is shown in the tables. See Section 5.3 for further discussion on this issue. We discuss only the results from the `borus02` and `UXCLUMPY` models because they are consistent with the `borus02`* and `MYTorus` results and the latter two models were only used as a consistency check for the former. The

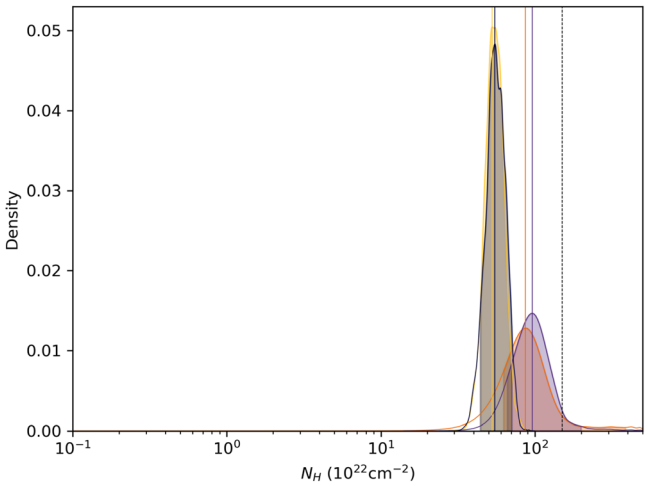

Figure 3. Posterior probability distribution of the line-of-sight $N_{\rm H,l.o.s}$ of CGCG 1822.3+2053 for both models and both observations. The solid vertical lines indicate the most probable value for $N_{\rm H,l.o.s}$ and the shaded regions indicate the 90% credible interval for the $N_{\rm H,l.o.s}$ measurement. The colors orange and purple correspond to the Chandra observations fit with the `borus02` model and the `UXCLUMPY` model, respectively. The colors yellow and blue correspond to the XMM-Newton observations fit with the `borus02` model and the `UXCLUMPY` model, respectively. The dashed vertical line indicates the CT threshold.

results for CGCG 1822.3+2053are shown in this section (Figures 2–4), while the results for the other sources are shown in the Appendix (Figures 7–17).

4.1. 2MFGC 9836

2MFGC 9836 was classified as a Seyfert 2 galaxy by Y.-P. Chen et al. (2022) based on optical spectroscopy. The source was observed with Chandra in December of 2021 for 10 ks. We ignored channels in the Swift-BAT data that had a count rate consistent with zero and were much lower than the rest of the data because they affected the fitting of the photon index. The Chandra spectrum was fitted in the energy range 1–7 keV.

The X-ray spectrum shows an obscured but decidedly Compton-thin nature. While the $N_{\rm H,l.o.s}$ is measured quite precisely, the torus parameters remain unconstrained in both models. The best-fit parameters and errors for both models and methods are shown in Table 5. The $N_{\rm H,l.o.s}$ posteriors from the nested sampling and the contours from the LM fit along with the best-fit spectra are shown in Figure 7. The corner plots for both models are shown in Figure 12. There is a 0.0% probability of the data being CT for both models according to the $N_{\rm H,l.o.s}$ posteriors. We classify this source as an obscured, Compton-thin AGN.

4.2. NGC 5759

NGC 5759 is part of a galaxy pair with LEDA 200319. The source was observed with XMM-Newton in August of 2021 for 15 ks and with Chandra in September of 2022 for 10 ks. The soft X-ray emission from LEDA 200319 is primarily below 1 keV. By extrapolating a power-law model from the data, the 15–150 keV flux is estimated to be around a factor of 1000 less than the flux of NGC 5759. Therefore, we assume negligible contamination in the Swift-BAT spectrum from LEDA 200319. The Chandra data were fitted in the energy range 1–7 keV, while the XMM-Newton data were fitted in the energy range 1–8 keV. The spectrum shows a heavily obscured nature. The best-fit parameters and errors for both models and methods are shown in Table 6. The $N_{\rm H,l.o.s}$ posteriors from the nested sampling and the contours from the LM fit along with the best-fit spectra are shown in Figure 8. The corner plots for both models are shown in Figure 13.

The XMM-Newton observation yields a lower limit near the CT threshold in both the contours and the posterior distributions. The posteriors for the Chandra data are largely consistent with a CT solution with more than half of the probability mass being in the CT regime. However, the LM contours have a greater confidence in a Compton-thin solution. The posteriors for the Chandra data show a 59.1% and 60.6% probability of being CT according to the `borus02` and `UXCLUMPY` models, respectively. The posteriors for the XMM-Newton data show a 84.1% and 86.3% probability. This source is the best CT candidate in the present sample and future NuSTAR data from cycle 10 (ID: 10209, P.I. Cox) will help confirm this result. Given the current data, we classify this source as an obscured, CT AGN candidate.

4.3. IC 1141

IC 1141 is classified as a low-ionization nuclear emission-line region (LINER) based on SDSS spectroscopic data (Y. Toba et al. 2014). The source was observed in July of 2023 with Chandra for 10 ks and in 2022 February with XMM-Newton for 13 ks. The XMM-Newton data are very poor quality due to a flare occurring throughout the observation. As a result, we use only the Chandra and Swift-BAT data in our analysis. The Chandra data were fitted in the energy range 1–7 keV.

The X-ray spectrum shows a moderately obscured nature. The best-fit parameters and errors for both models and methods are shown in Table 7. The $N_{\rm H,l.o.s}$ posteriors from the nested sampling and the contours from the LM fit along with the best-fit spectra are shown in Figure 9. The corner plots for both models are shown in Figure 14. Based on the $N_{\rm H,l.o.s}$ posteriors, there is a 5.5% and 4.4% probability of the source being CT according to the `borus02` and `UXCLUMPY` models, respectively. We classify this source as an obscured, Compton-thin AGN.

4.4. 2MASX J17253053–4510279

2MASX J17253053–4510279 is an AGN that has been previously classified as a Seyfert 2 galaxy (M. J. Koss et al. 2022). A. Malizia et al. (2023) classified it as a LINER galaxy that is most likely type 1 despite WISE data showing an unusually blue W1 − W2 color (0.36) that can be indicative of absorption in AGN. They found it to be unabsorbed in the X-rays and noted the presence of a broad He I line (F. Ricci et al. 2022) leading to their classification of type 1.

The source was observed in 2021 October with XMM-Newton for 14.6 ks and in 2022 October with Chandra for 10 ks. The Chandra data were fitted in the energy range 1–7 keV while the XMM-Newton data were fitted in the energy range 1–9 keV. The best-fit models along with the $N_{\rm H,l.o.s}$ posteriors from the nested sampling and the contours from the LM fit are shown in the Appendix. As can be seen, the spectrum is unabsorbed. For this reason, we decided to remove the scattering component from the model and freeze all of the torus parameters because they could not be constrained and

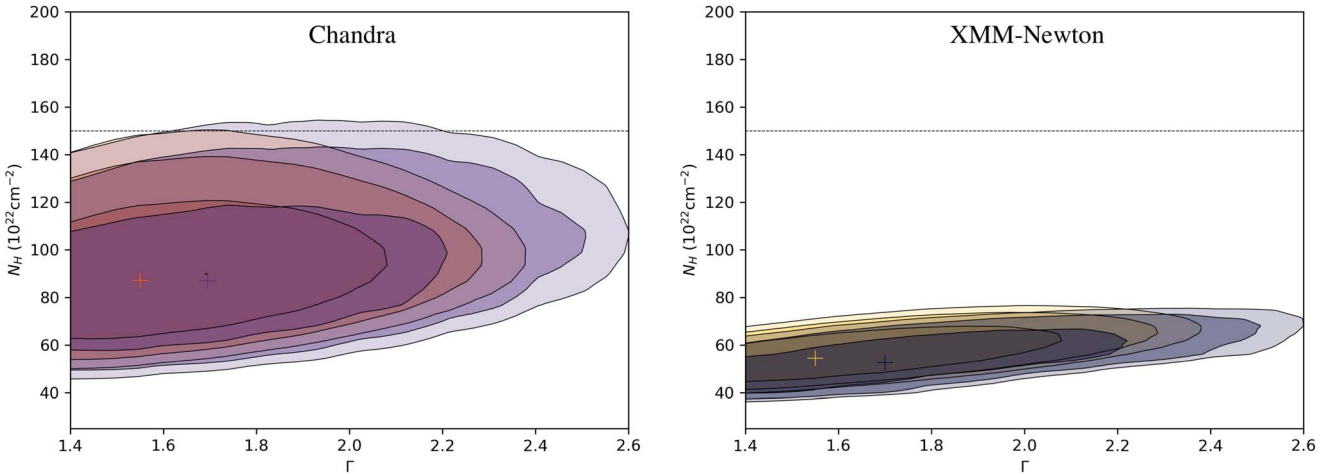

Figure 4. CGCG 1822.3+2053. Contour plots for line-of-sight column density and photon index obtained with the `steppar` command in `XSPEC`. Left-hand panel: Results for the Chandra observation. The `borus02` model results are in orange and the `UXCLUMPY` model results are in purple. The contours correspond to the 68%, 90%, and 95% confidence levels. Right-hand panel: Results for the XMM-Newton observation. The `borus02` model results are in yellow and the `UXCLUMPY` model results are in blue. The contours correspond to the 68%, 90%, and 95% confidence levels. The dashed horizontal line indicates the CT threshold.

caused the default model to be too computationally intensive for the Bayesian analysis.

The best-fit parameters and errors for both models and methods are shown in Table 8. The $N_{\rm H,l.o.s}$ posteriors from the Bayesian analysis and the contours from the LM fit along with the best-fit spectra are shown in Figure 10. The corner plots for both models are shown in Figure 15. There is a 0.0% probability of the data being CT for both models according to the $N_{\rm H,l.o.s}$ posteriors. We classify this source as a Type 1 AGN. Interestingly, there is a strong hint of variability in the obscuration between the Chandra and XMM-Newton observations, even though both epochs have $N_{\rm H,l.o.s} < 10^{22}$ cm^{-2}. The $N_{\rm H,l.o.s}$ is fairly well constrained in the Chandra data, whereas the XMM-Newton data provide an upper limit around the Galactic absorption, indicated by the dashed horizontal line in the contour plot of Figure 10.

Another interesting thing to note about this source is the large difference in the cross-normalization between observations, indicating flux variability. The fits show that the XMM-Newton cross-normalization is ~2 times higher than Chandra, while the Swift-BAT cross-normalization is ~3–4 times higher than Chandra. Since the Swift-BAT flux should result in the average flux of the source over the 157 months, our soft X-ray observations, which are a full year apart, both occurred during a relatively low flux state. This also implies that the source must have been in a much higher flux state at some point during the 157 months of Swift-BAT integration time. The Swift-BAT light curve[13] indeed shows evidence of variability in the 14–195 keV flux. The source is quite faint, so we used a weighted average to rebin the light curve to ~yearly bins which shows the source varies on the order of 1 mCrab (~2×10^{-11} erg/s/cm^{-2}). A chi-square test assuming a constant flux results in a p-value of 0.03, indicating flux variability in the hard X-rays. The variable nature of this source could be the reason why this source was selected as a potentially obscured AGN. Given the current data, we decide to classify this source as an unobscured, potentially $N_{\rm H,l.o.s}$-variable AGN.

[13] The light-curve data are available at https://swift.gsfc.nasa.gov/results/bs157mon/1504.

4.5. CGCG 1822.3+2053

CGCG 1822.3+2053 was observed in July of 2022 with Chandra for 10 ks and in September of 2021 with XMM-Newton for 10 ks. The Chandra data were fitted in the energy range 1–7 keV, while the XMM-Newton data were fitted in the energy range 1–9 keV. The spectrum shows a moderately obscured nature. The spectral fits with `borus02` and `UXCLUMPY` are shown in Figure 2. The $N_{\rm H,l.o.s}$ posteriors are shown in Figure 3 and the contours are shown in Figure 4. Table 4 shows the best-fit parameters and their errors for both models and both methods, along with the intrinsic luminosity and the observed flux in cgs units. The corner plots for both models are shown in Figure 16.

The measured $N_{\rm H,l.o.s}$ for the Chandra data is consistent with being CT at 90% confidence. The torus parameters are unconstrained; however, the obscured nature of the source is confidently confirmed. Based on the current Chandra posteriors, there is a 18.3% and 10.4% probability of the source being CT according to the `borus02` and `UXCLUMPY` models, respectively. Both model posteriors confidently assert a Compton-thin scenario for the XMM-Newton data with a 0.0% probability of being CT. We classify this source as an obscured, Compton-thin AGN. Future NuSTAR data from Cycle 10 will help determine whether the source is Compton-thin or CT, as well as provide tighter constraints on the torus parameters.

4.6. MCG +2-57-2

MCG +2-57-2 was classified as a Seyfert 1.9 by K. L. Smith et al. (2020). It was observed with Chandra in November of 2021 for 10 ks. The spectrum is piled up, which we account for by using the algorithm developed by J. E. Davis (2001) and implemented in `XSPEC` as `pileup`. The Chandra data were fitted in the energy range 1–7 keV. Both models and fitting methods agree that the spectrum is unobscured. The best-fit parameters and errors for both models and methods are shown in Table 9. The $N_{\rm H,l.o.s}$ posteriors from the nested sampling and the contours from the LM fit along with the best-fit spectra are shown in Figure 11. The corner plots for both models are shown in Figure 17. There is a 0.0% probability of the data

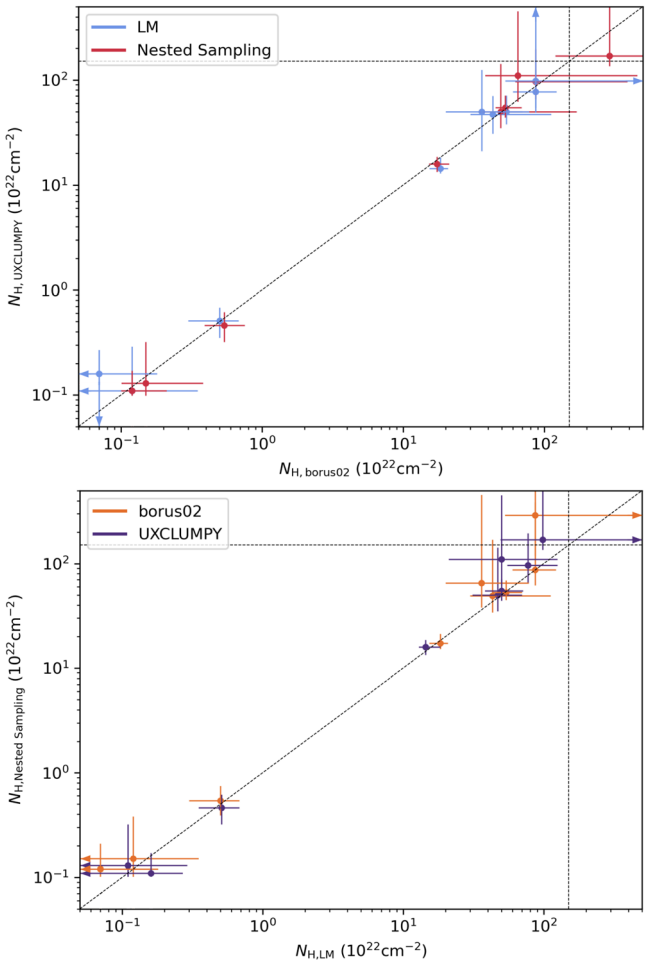

Figure 5. Top panel: Comparison of the $N_{\rm H,l.o.s}$ measured with the UXCLUMPY model against the measured $N_{\rm H,l.o.s}$ with the borus02 model. The values obtained with least squares fitting are shown in blue, while the most probable values obtained through Bayesian fitting are shown in red. Bottom panel: Comparison of the $N_{\rm H,l.o.s}$ measured with least squares fitting against the most probable $N_{\rm H,l.o.s}$ from Bayesian fitting. The borus02 values are shown in orange and the UXCLUMPY values are shown in purple. The dashed lines in both panels indicate the CT threshold.

being CT for both models according to the $N_{\rm H,l.o.s}$ posteriors. We classify this source as an unobscured AGN.

5. Discussion

We have used two different models (borus02 and UXCLUMPY) and two different methods (least squares and Bayesian regression) to estimate the line-of-sight $N_{\rm H}$ in six local AGN. In this section, we compare the results of the two models and methods, and show that the $N_{\rm H,l.o.s}$ estimates are reliable. Furthermore, we check the sources with multiple soft X-ray observations for variability in absorption. We also discuss the discrepancy between the most probable parameter values obtained from the posterior distributions and the parameter values resulting in the maximum likelihood spectral fit.

5.1. Comparison of $N_{H,l.o.s}$ Determinations

The borus02 model only includes the reprocessed emission and does not include the primary power law that gets absorbed by the torus. We obtain the line-of-sight $N_{\rm H}$ by adding an absorbed power law to the borus02 model and untying this $N_{\rm H}$ from the average column density $N_{\rm H,avg}$ to account for the fact the torus is likely inhomogeneous. In the UXCLUMPY model, the line-of-sight $N_{\rm H}$ can be calculated within the model because the total absorption depends on the number of clouds in the line of sight.

Figure 5 shows the measured $N_{\rm H,l.o.s}$ values between the two different models and methods. The top panel shows excellent agreement in $N_{\rm H,l.o.s}$ between the borus02 and UXCLUMPY models, despite the different assumptions. This is in agreement with the results of, for example, A. Pizzetti et al. (2022) and N. Torres-Albà et al. (2023), which show similar consistency in the measurements of $N_{\rm H,l.o.s}$ from different models, even when using large data samples and multiple observations.

The bottom panel shows a relatively good agreement between methods; however, there are a few instances where the lower limit of the nested sampling algorithm is higher than the best-fit value from the LM algorithm. This is likely due to the way we define the "best" value and credible interval with the Bayesian technique. In general, the highest probability value in the posterior distribution is not the same as the value that gives the maximum likelihood (see Section 5.3). For example, the highest orange point in the bottom panel of Figure 5 shows the borus02 measurement for the XMM-Newton observation of NGC 5759. The posterior provides a 90% credible interval that is inconsistent with the $N_{\rm H,l.o.s}$ value that provides the maximum likelihood. The maximum likelihood value of $N_{\rm H,xmm} = 94 \times 10^{22}\,{\rm cm}^{-2}$ is in much better agreement with the value obtained through least squares fitting. Furthermore, the LM fit value is a lower limit, so it is still consistent with the nested sampling determined value.

There also seems to be a hint that the Bayesian regression favors higher $N_{\rm H,l.o.s}$; however, these cases are all at high obscuration where it is easier to constrain the lower limit on the obscuration leaving more mass in the upper end of the posterior. Furthermore, there are not enough data points here to indicate that this is even a real difference in the methods, so we conclude that the methods are consistent.

5.2. $N_{H,l.o.s}$ Variability

We conduct an obscuration variability analysis on the three sources with two soft X-ray observations. We obtain a "probability of variation," $P_{\rm var}$, from the $N_{\rm H,l.o.s}$ posterior distributions for each model. We define this probability as

$$P_{\rm var} = \left(1 - \frac{|N_{\rm H,cha} \cap N_{\rm H,xmm}|}{|N_{\rm H,cha}| + |N_{\rm H,xmm}|}\right) \times 100$$

where $N_{\rm H,cha}$ is the set of points in the $N_{\rm H,l.o.s}$ posterior returned by BXA for the Chandra observation and $N_{\rm H,cha}$ is the XMM-Newton observation. In words, this is the percentage of posterior mass uncommon to the two distributions.

Using this definition, we find that 2MASX J17253053–4510279 has the highest probability of being variable with $P_{\rm var} = 89\%$ for both borus02 and UXCLUMPY. For CGCG 1822.3+2053, we obtain $P_{\rm var} = 28\%$, 30% for borus02 and UXCLUMPY, respectively. For NGC 5759, we obtain $P_{\rm var} = 4\%$, 3%. All three of these sources will be observed simultaneously with NuSTAR and XMM-Newton, giving us a third observation to test for variability.

5.3. Bayesian Posterior Distributions

The final result of the Bayesian analysis is the posterior distribution for each parameter. This result contains all of the information that we can obtain about a given parameter of interest with the available data and prior knowledge of that parameter. However, it is not immediately clear how to interpret this distribution. For example, can a single value (e.g., the mean, median, or mode) with associated uncertainty describe a given posterior distribution well? For well-behaved parameter spaces with mono-modal, symmetric (e.g., Gaussian) posterior distributions, this question does not matter since the mean, median, and mode will be equivalent. However, as can be seen in the 1D histograms on the diagonal of the corner plots in Figures 12–15, many of the posterior distributions do not have Gaussian shapes. We decided to report the mode and associated interquartile range of the posterior distribution for all parameters, but caution the reader against over-interpreting these values without visually inspecting the 1D histogram shapes first.

One related issue that we would like to highlight in particular arises from using the mode of a given posterior parameter distribution as a "best-fit" when the parameter is in fact unconstrained. The immunity of BXA to local minima means that if a posterior is found to be unconstrained, i.e., not significantly different from its corresponding prior, a single parameter value should not be favored as a best-fit relative to the remaining unconstrained portion of the parameter space. There are cases where using the mode of all (including unconstrained) posteriors results in a bad fit for this reason, and underlines the importance of mapping out interparameter dependencies fully rather than relying on individual parameter vectors to describe a fit.

To illustrate this, we calculated the percent difference between the mode of the posterior distribution and the best-fit value for each parameter. In Figure 6, we plotted this difference against the relative entropy (also called the Kullback–Leibler divergence or the information gain) (S. Kullback & R. A. Leibler 1951) between the posterior and the prior. We use the equation

$$\text{Relative Entropy} = \int_{-\infty}^{\infty} P(x) \log_2 \left(\frac{P(x)}{\pi(x)} \right) dx$$

where $P(x)$ is the posterior distribution and $\pi(x)$ is the prior distribution. The logarithm is base 2, which provides the relative entropy in units of bits. We obtain $P(x)$ by applying a Gaussian kernel density estimator with the bandwidth selected using Scott's Rule[14](D. W. Scott 2015). We implement this with the `Gaussian_kde` function in SciPy (P. Virtanen et al. 2020) and the code and data used for the values in Figure 6 are provided in I. Cox (2024). We define the uniform prior distribution as $\pi(x) = (b - a)^{-1}$ and the log-uniform prior distribution as $\pi(x) = [x \log(b/a)]^{-1}$ where a and b are the lower and upper bounds of the prior range, respectively. Essentially, the relative entropy quantifies the difference between two distributions, which in this context means the degree to which the data were able to constrain a parameter relative to the initially assumed prior. High relative entropy values indicate a well constrained parameter while low relative entropy values mean the data are consistent with a large percentage of the prior range. At a glance, Figure 6 shows that when the parameter is well constrained (relative entropy $\gtrsim$1 bit[15]), there is good agreement between the posterior mode and the best-fit value. However, as the parameter becomes more unconstrained, the scatter increases greatly. An important conclusion that we can draw from this is that one should be wary of any singular number obtained from the posterior distribution, especially when the relative entropy is less than a few bits. In the extreme cases (relative entropy $\ll$1 bit), the most probable value is simply a random draw from the prior and contains no useful information. The advantage of having the posterior distribution and relative entropy is that it shows clearly when the fit is insensitive to the parameter, whereas LM can struggle to do this.

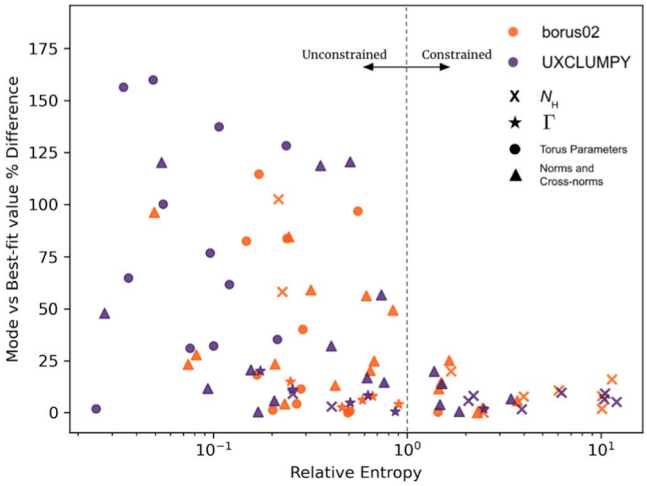

Figure 6. The percent difference between the mode of the posterior distribution and the best-fit value for each parameter plotted against the relative entropy of the posterior and prior distributions in bits. The relative entropy quantifies how tightly constrained the measurement of a parameter is relative to its prior. The orange points are parameters in the `borus02` model and the purple points are parameters in the `UXCLUMPY` model. The "x" markers indicate the $N_{\rm H,l.o.s}$, the star markers indicate the photon index, the triangle markers indicate normalization and cross-normalization parameters, and the circle markers indicate the torus geometry parameters.

Furthermore, these results show that in most cases the data are able to greatly constrain the $N_{\rm H,los}$ despite not being able to constrain any of the torus geometry parameters, which need high quality NuSTAR data to properly measure.

6. Summary

In this paper, we have provided the first analysis of soft X-ray data for five hard X-ray sources selected from the Palermo BAT 150 month catalog and one from the 157 month catalog. These sources were selected as likely obscured candidates due to the lack of a soft X-ray ROSAT counterpart. We obtained snapshot images with Chandra and estimated the line-of-sight column density, $N_{\rm H,l.o.s}$, to find CT candidates. These candidates will be followed up with simultaneous NuSTAR and XMM-Newton data in an effort to catalog all of the CT AGN in the local universe and to

[14] Scott's Rule can lead to oversmoothing for multimodal distributions; however, none of the parameters shown in Figure 6 demonstrate obvious multimodal behavior so this should not be an issue.

[15] For reference, a Gaussian distribution whose width shrinks by a factor of 3 between the prior and posterior would have a relative entropy of 1 bit (J. Buchner 2022).

better understand the nature of the obscuring medium that is colloquially known as the torus. We find that two of our sources (2MASX J17253053–4510279 and MCG +2-57-2) are likely unobscured. The rest of our sources are obscured, with two of them (CGCG 1822.3+2053 and NGC 5759) showing a nonzero probability of being CT. We classify these two sources as CT candidates, with NGC 5759 being the strongest between the two.

We used two physically motivated models to fit the hard and soft X-ray data for each source and we compare the $N_{\rm H,l.o.s}$ measurements obtained with both. Since the data quality did not allow strong constraints in the torus parameters of these two models, we fitted with simpler models as well to confirm the $N_{\rm H,los}$ measurements. We also use least squares and Bayesian fitting methods for each source and model to compare the results. We find that the $N_{\rm H,l.o.s}$ measurements are in good agreement between all models and both fitting methods.

We also consider the interpretation and reliability of values obtained from the posterior distribution obtained by nested sampling. We find that for unconstrained parameters with a low relative entropy between the posterior distribution and prior distribution, the most probable value according to the posterior distribution can be very different from the value that provides the best fit. Therefore, in most cases, the posterior distribution should be considered in conjunction with the best-fit value, and individual numbers derived from the posterior should be treated with caution. However, in general, the posterior distribution is still consistent with the best-fit values within a 90% credible interval.

Three sources have two soft X-ray observations and we look for variability in the $N_{\rm H,l.o.s}$ between the two observations. We find little evidence of $N_{\rm H,l.o.s}$ variability in CGCG 1822.3+2053 and NGC 5759; however, 2MASX J17253053–4510279 does show a strong hint of variability despite being only marginally obscured.

Three sources have been approved for simultaneous NuSTAR and XMM-Newton observations (2MASX J17253053–4510279, CGCG 1822.3+2053, and NGC 5759) in NuSTAR Cycle 10 (ID: 10209, P.I. Cox). These data, in conjunction with Swift-BAT, will provide continuous spectral coverage from 1 to 150 eV, with a much clearer view at energies ~20 keV where the reflection is more important. These observations will help confirm the results shown here, provide a third observation for each of the sources to study variability, and better constrain the torus parameters. These results will be presented in a future publication (I. Cox et al. 2024, in preparation).

Acknowledgments

I.C. and N.T.A. acknowledge support under contracts GO2-23072X, G04-25065X, and 80NSSC23K1611. The scientific results reported in this article are based on observations made by the X-ray observatories Chandra XMM-Newton and Swift-BAT, and has made use of the NASA/IPAC Extragalactic Database (NED), which is operated by the Jet Propulsion Laboratory, California Institute of Technology under contract with NASA. We acknowledge the use of the software package HEASoft.

Appendix
Best Fits

In this appendix we present the results for all sources in the sample. The following tables and plots are the same as Table 4 and Figures 2–4. Figures 7–11 show the best-fit spectra for both models along with the posterior distributions and contour plots. Figure 7 shows the results for 2MFGC 9836. Figure 8 shows the results for NGC 5759. Figure 9 shows the results for IC 1141. Figure 10 shows the results for 2MASX J17253053-4510279. Figure 11 shows the results for MCG +2-57-2.

Figures 12–17 show the corner plots with the contours for all free parameters in both models. Figure 12 shows the results for 2MFGC 9836. Figure 13 shows the results for NGC 5759. Figure 14 shows the results for IC 1141. Figure 15 shows the results for 2MASX J17253053-4510279. Figure 16 shows the results for CGCG 1822.3+2053. Figure 17 shows the results for MCG +2-57-2.

Tables 5–9 show the best fit parameters for both models and fitting methods. Table 5 shows the results for 2MFGC 9836. Table 6 shows the results for NGC 5759. Table 7 shows the results for IC 1141. Table 8 shows the results for 2MASX J17253053-4510279. Table 9 shows the results for MCG +2-57-2.

The luminosities shown are intrinsic and in units of erg s^{-1}, while the fluxes are observed and in units of erg cm^{-2} s^{-1}. In all plots, the color orange corresponds to the `borus02` fit to Chandra data. The color purple corresponds to the `UXCLUMPY` fit to Chandra data. The color yellow corresponds to the `borus02` fit to XMM-Newton data. The color blue corresponds to the `UXCLUMPY` fit to XMM-Newton data.

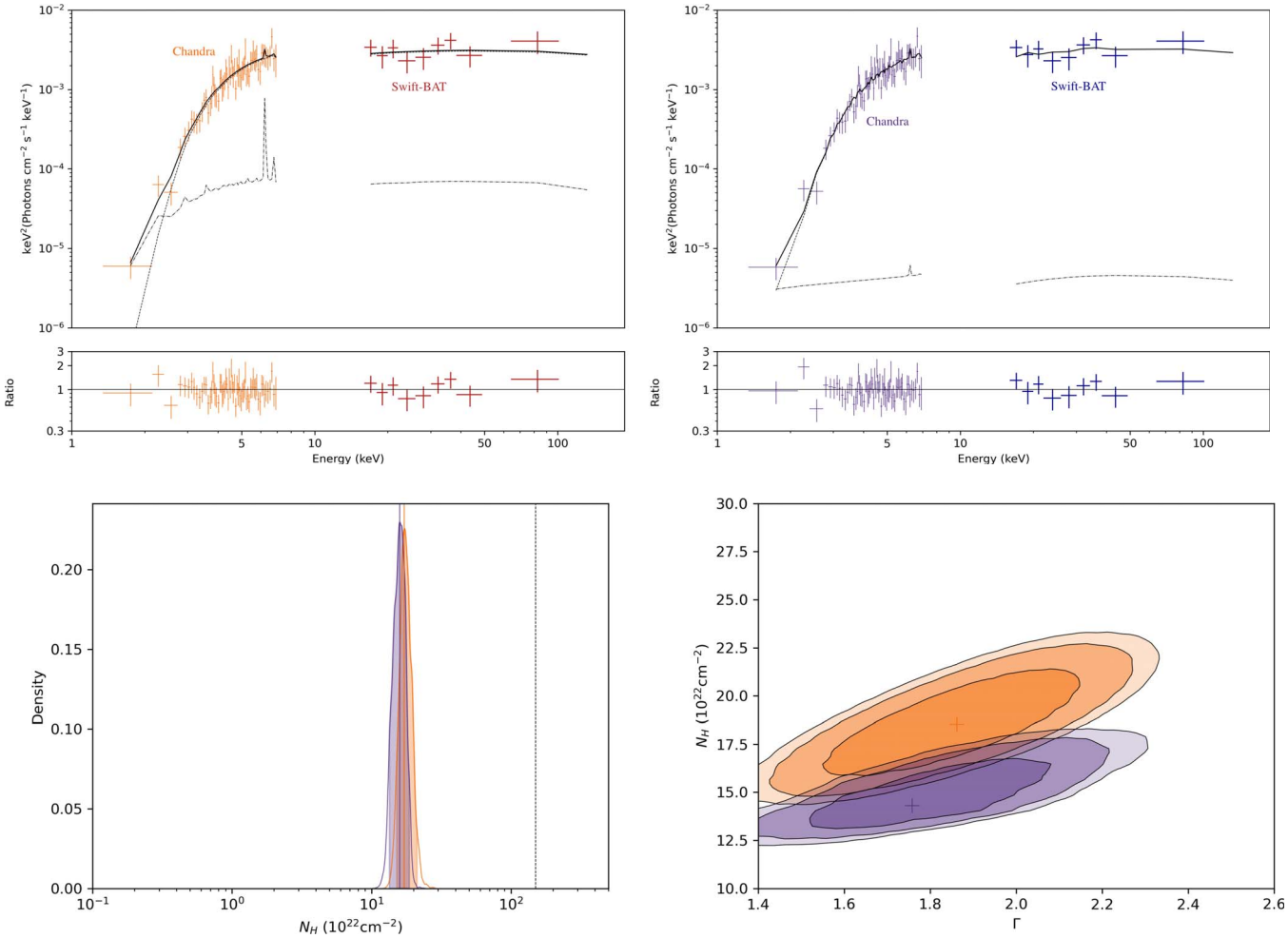

Figure 7. 2MFGC 9836. Top left-hand panel: Spectral fit for the `borus02` model. Top right-hand panel: Spectral fit for the `UXCLUMPY` model. Bottom left-hand panel: $N_{\rm H,l.o.s}$ posteriors for 2MFGC 9836. The `borus02` results are in orange and the `UXCLUMPY` results are in purple. Bottom right-hand panel: Contour plots of line-of-sight column density and photon index for 2MFGC 9836. The `borus02` results are in orange and the `UXCLUMPY` results are in purple.

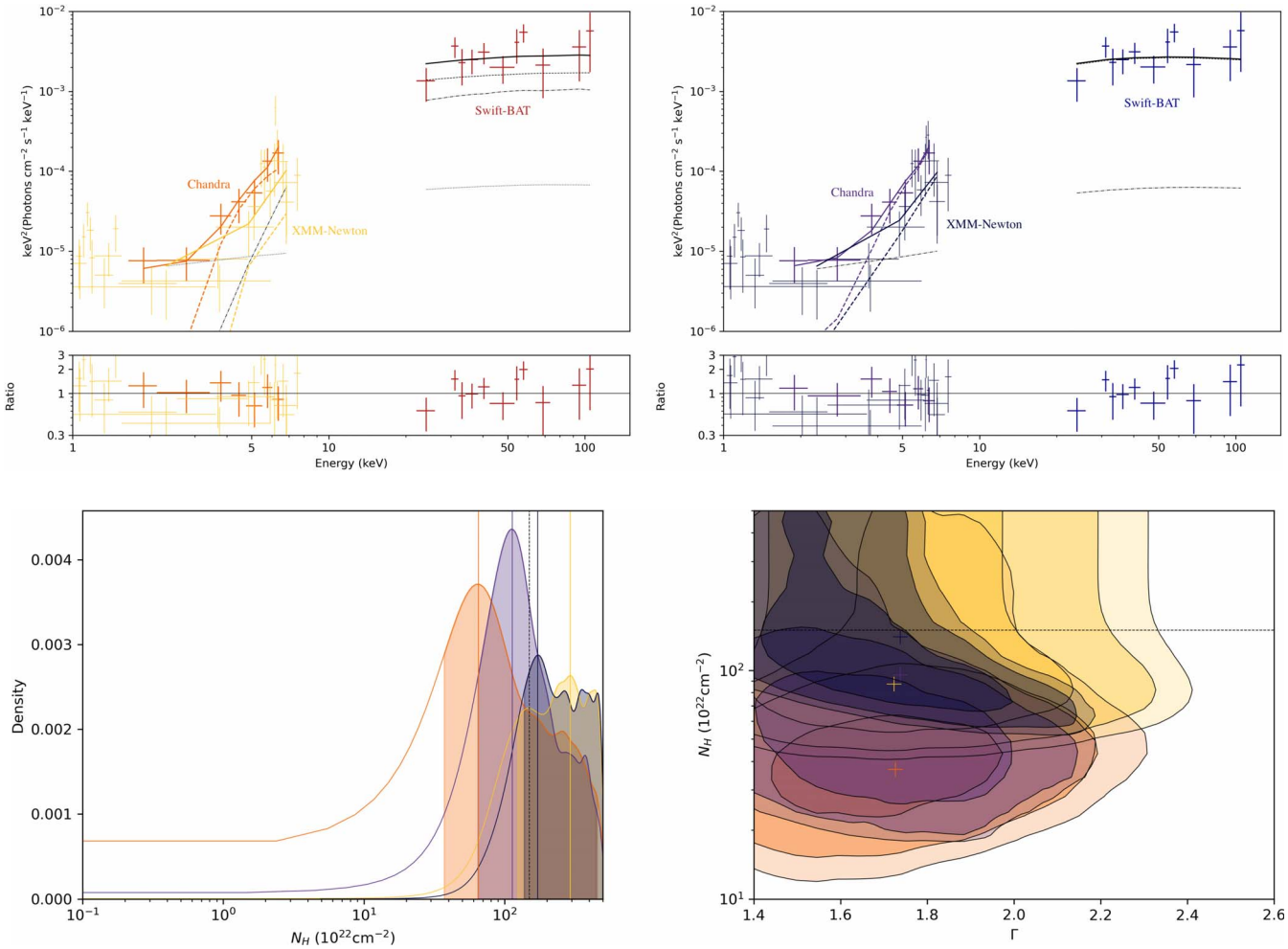

Figure 8. NGC 5759. Top panels: Same as Figure 2. Bottom left-hand panel: Same as Figure 3. Bottom right-hand panel: Same as Figure 4.

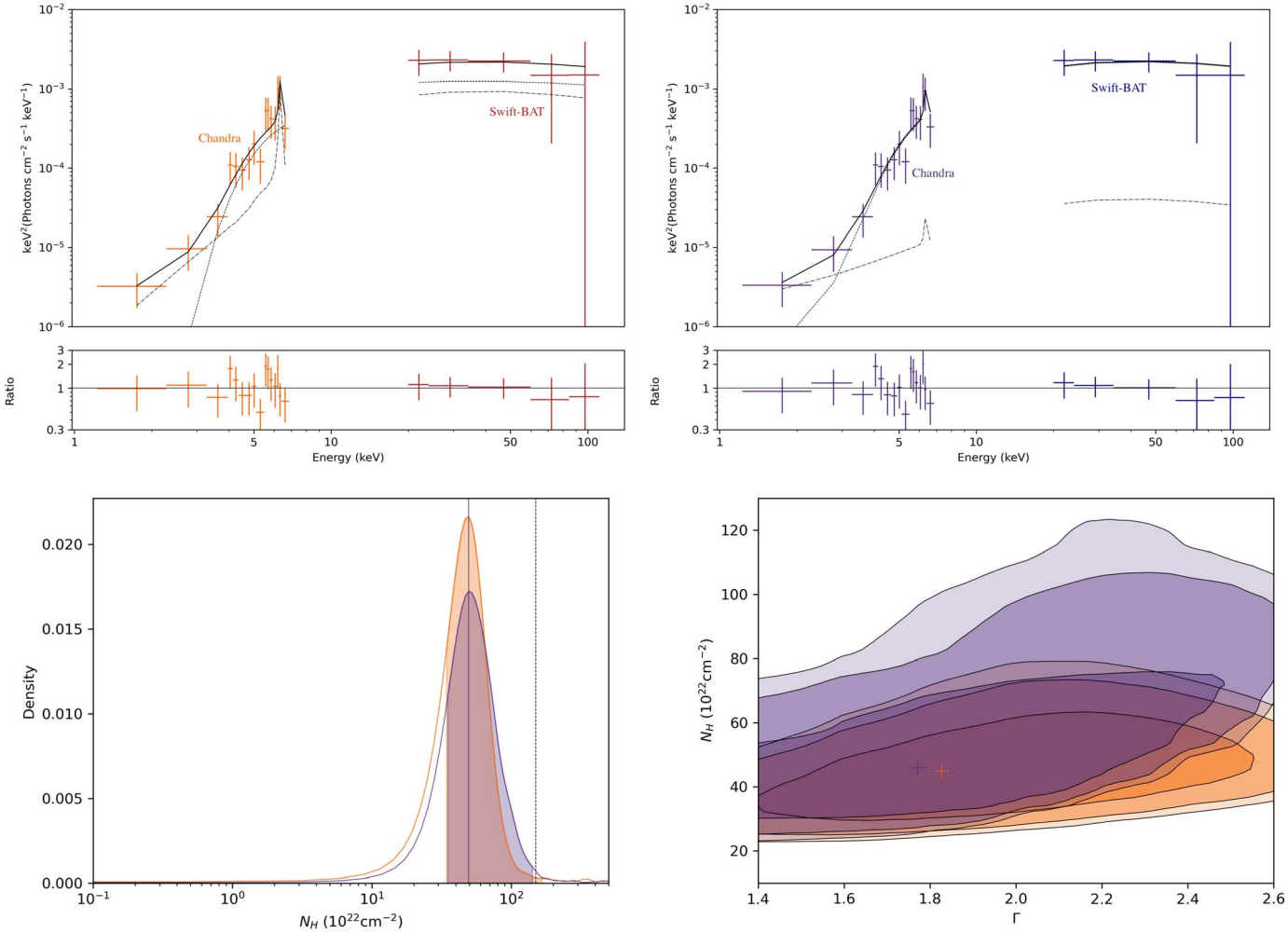

Figure 9. IC 1141. Top left-hand panel: Spectral fit for the `borus02` model. Top right-hand panel: Spectral fit for the `UXCLUMPY` model. Bottom left-hand panel: $N_{\mathrm{H,\,l.o.s}}$ posteriors for IC 1141. The `borus02` results are in orange and the `UXCLUMPY` results are in purple. Bottom right-hand panel: Contour plots of line-of-sight column density and photon index for IC 1141. The `borus02` results are in orange and the `UXCLUMPY` results are in purple.

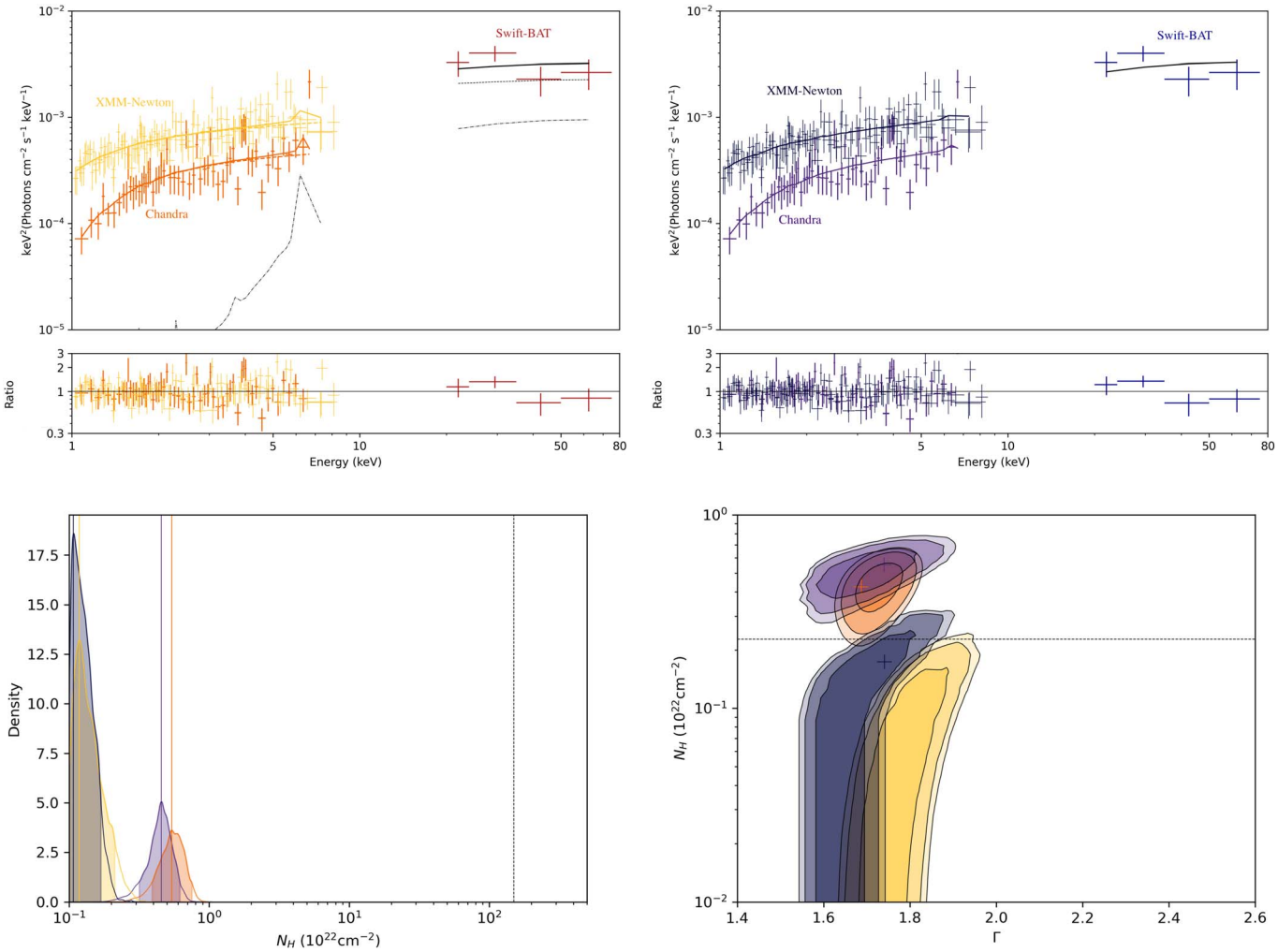

Figure 10. 2MASX J17253053–4510279. Top panels: Same as Figure 2. Bottom left-hand panel: Same as Figure 3. Bottom right-hand panel: Same as Figure 4.

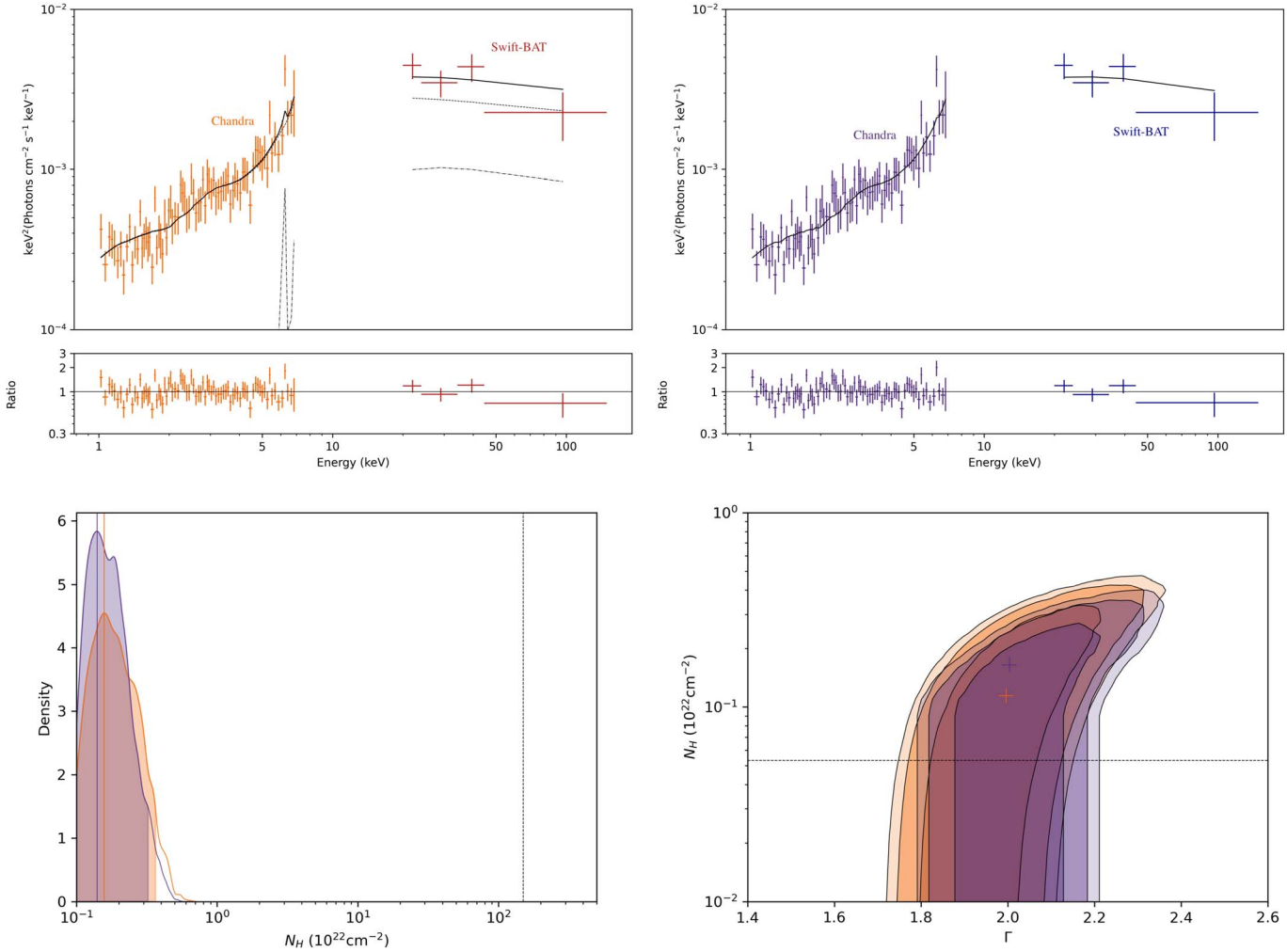

Figure 11. MCG +2-57-2. Top left-hand panel: Spectral fit for the `borus02` model. Top right-hand panel: Spectral fit for the `UXCLUMPY` model. Bottom left-hand panel: $N_{\rm H,l.o.s}$ posteriors for MCG +2-57-2. The `borus02` results are in orange and the `UXCLUMPY` results are in purple. Bottom right-hand panel: Contour plots of line-of-sight column density and photon index for MCG +2-57-2. The `borus02` results are in orange and the `UXCLUMPY` results are in purple. The hard spectral shape in the Chandra data is due to pileup.

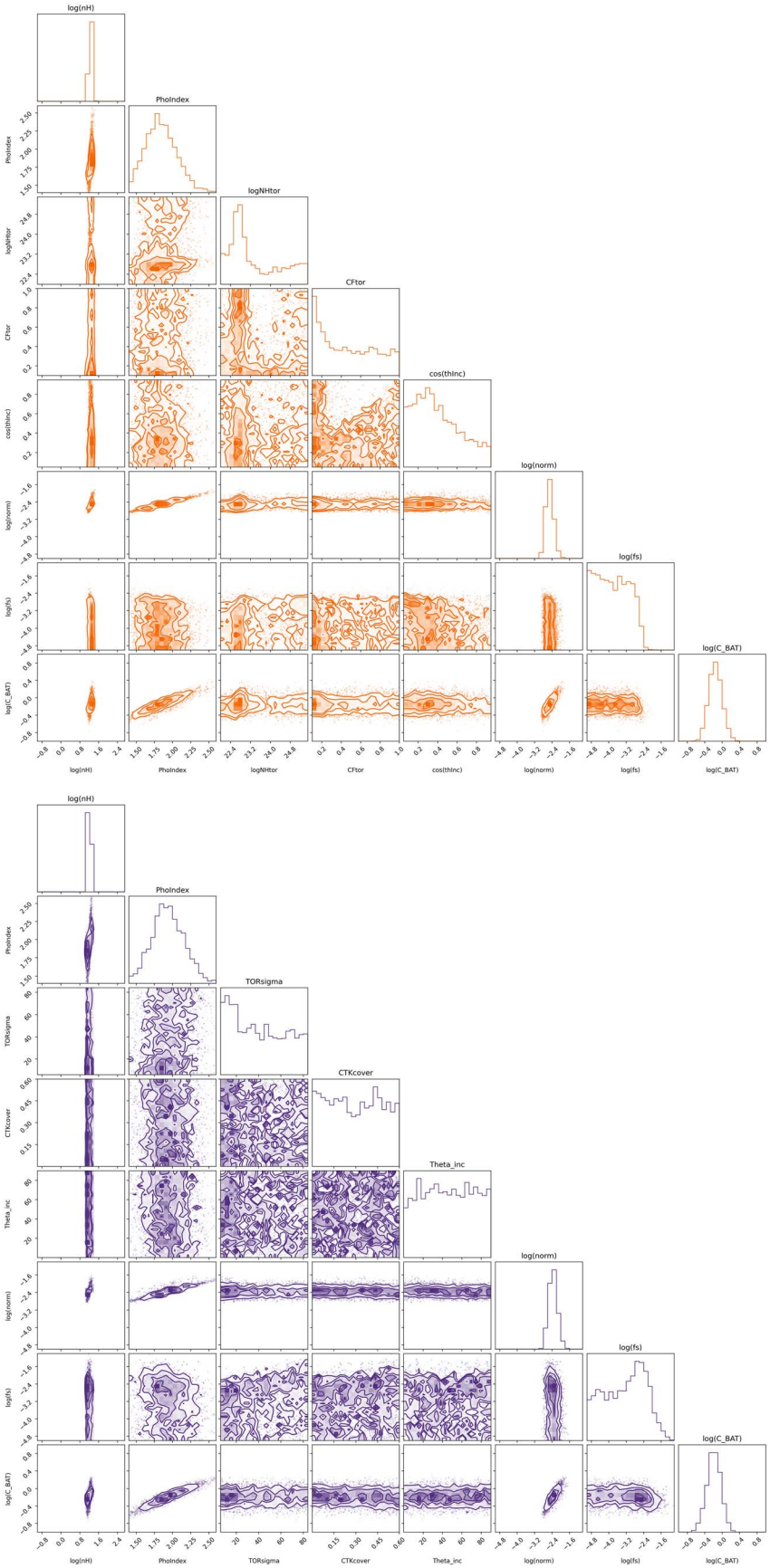

Figure 12. 2MFGC 9836. Top panel: Corner plot for the `borus02` model. Bottom left-hand panel: Corner plot for the `UXCLUMPY` model.

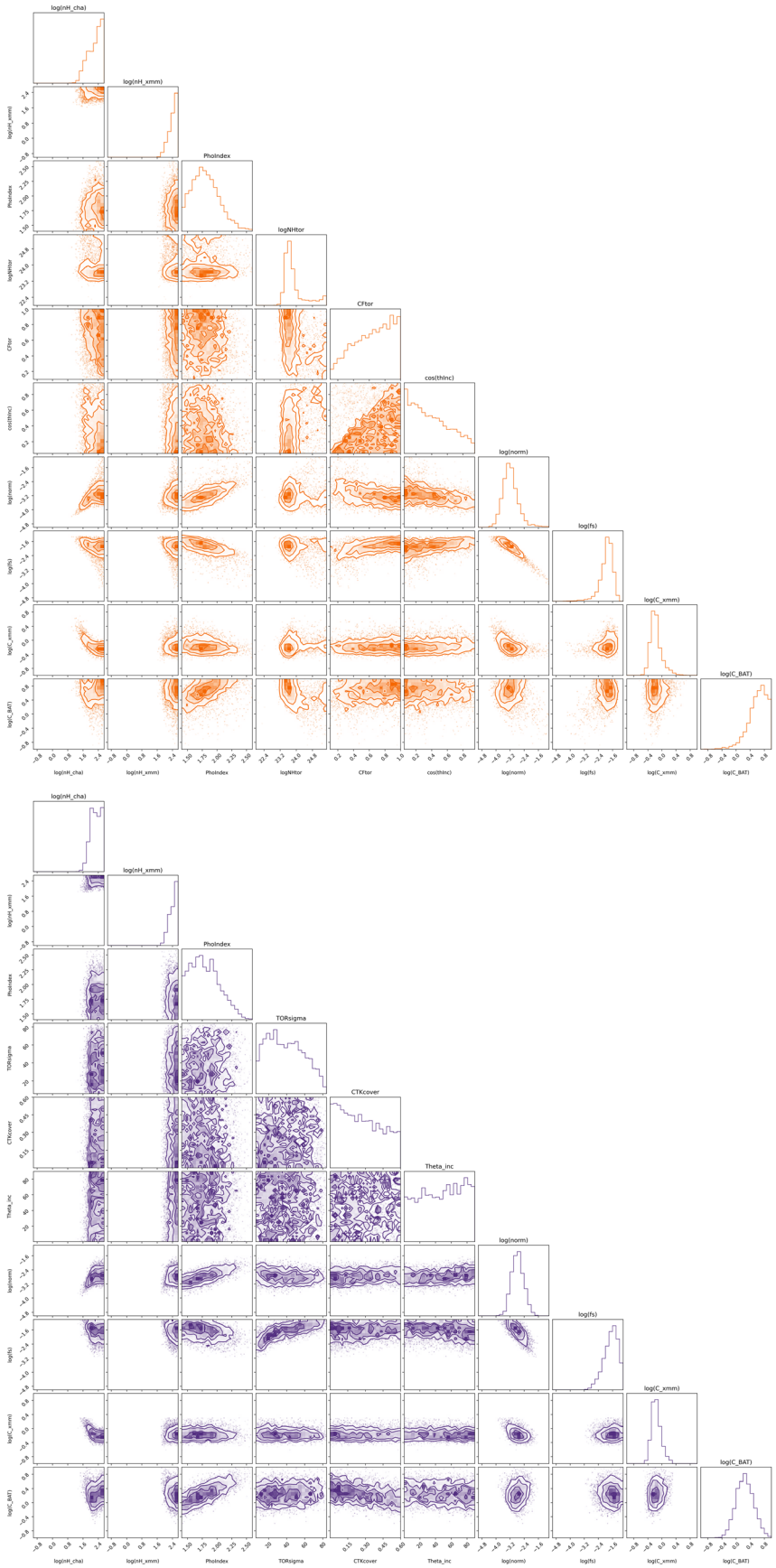

Figure 13. NGC 5759. Top panel: Corner plot for the `borus02` model. Bottom left-hand panel: Corner plot for the `UXCLUMPY` model.

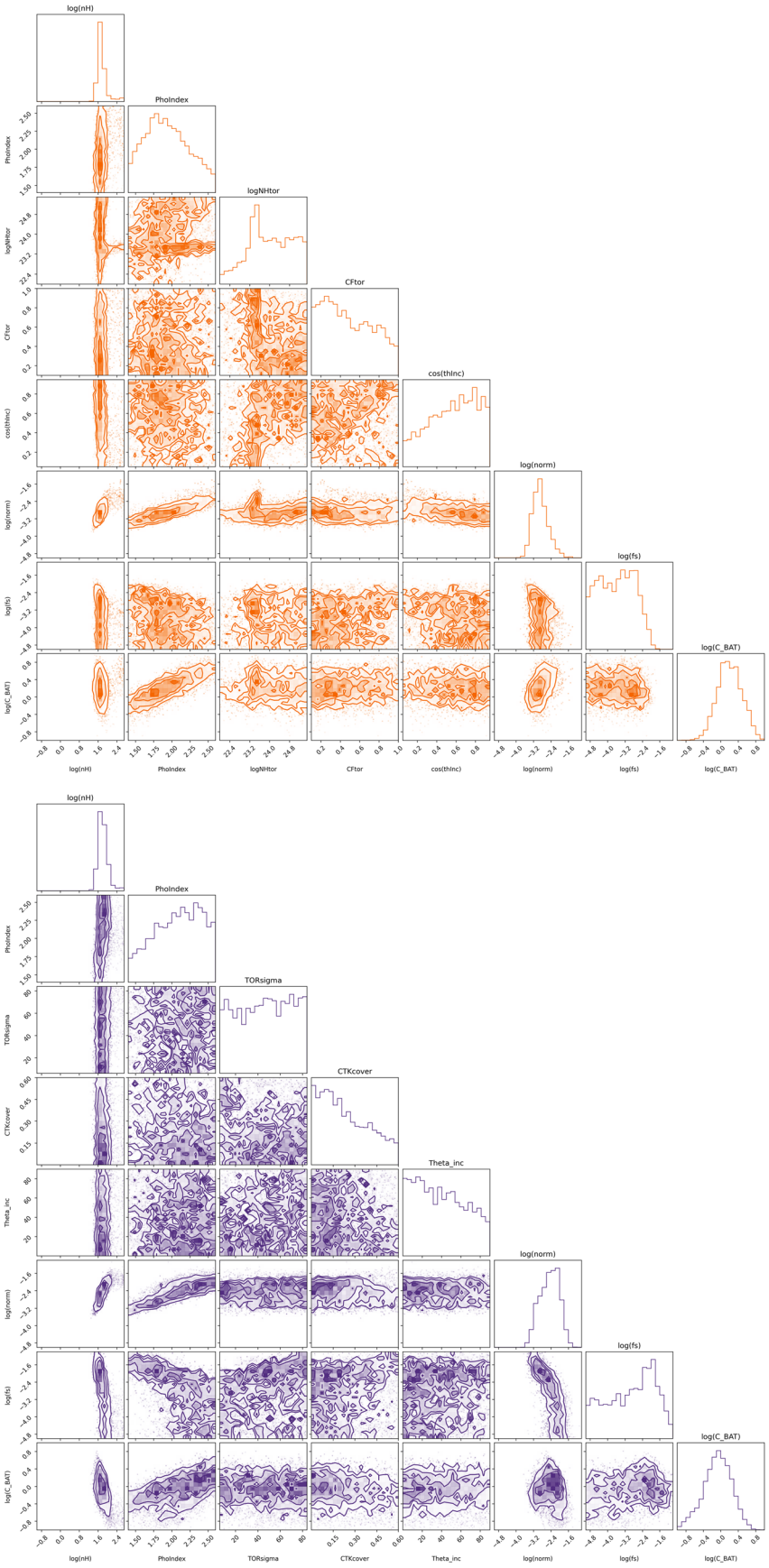

Figure 14. IC 1141. Top panel: Corner plot for the `borus02` model. Bottom left-hand panel: Corner plot for the `UXCLUMPY` model.

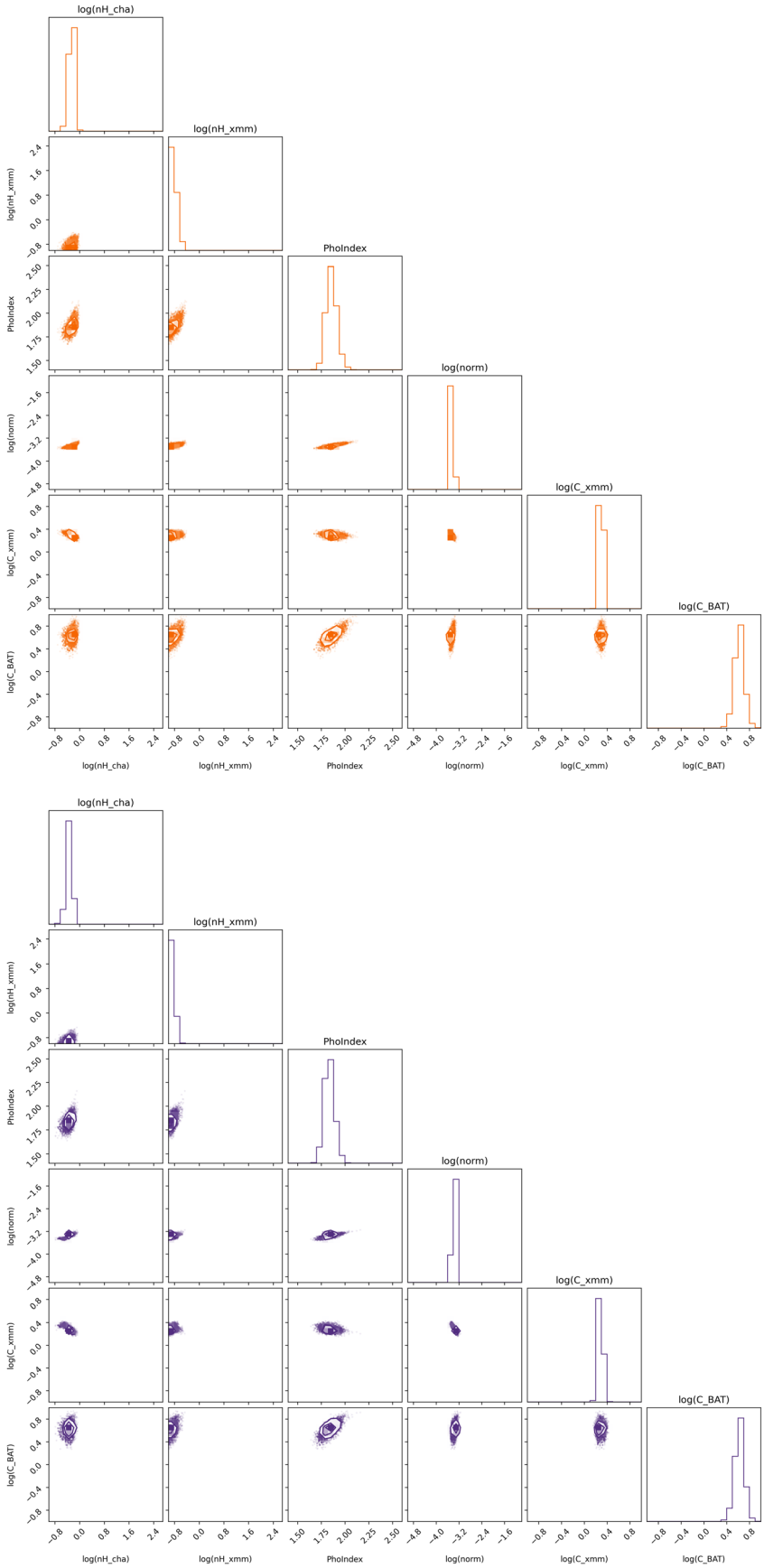

Figure 15. 2MASX J17253053–4510279. Top panel: Corner plot for the `borus02` model. Bottom left-hand panel: Corner plot for the `UXCLUMPY` model.

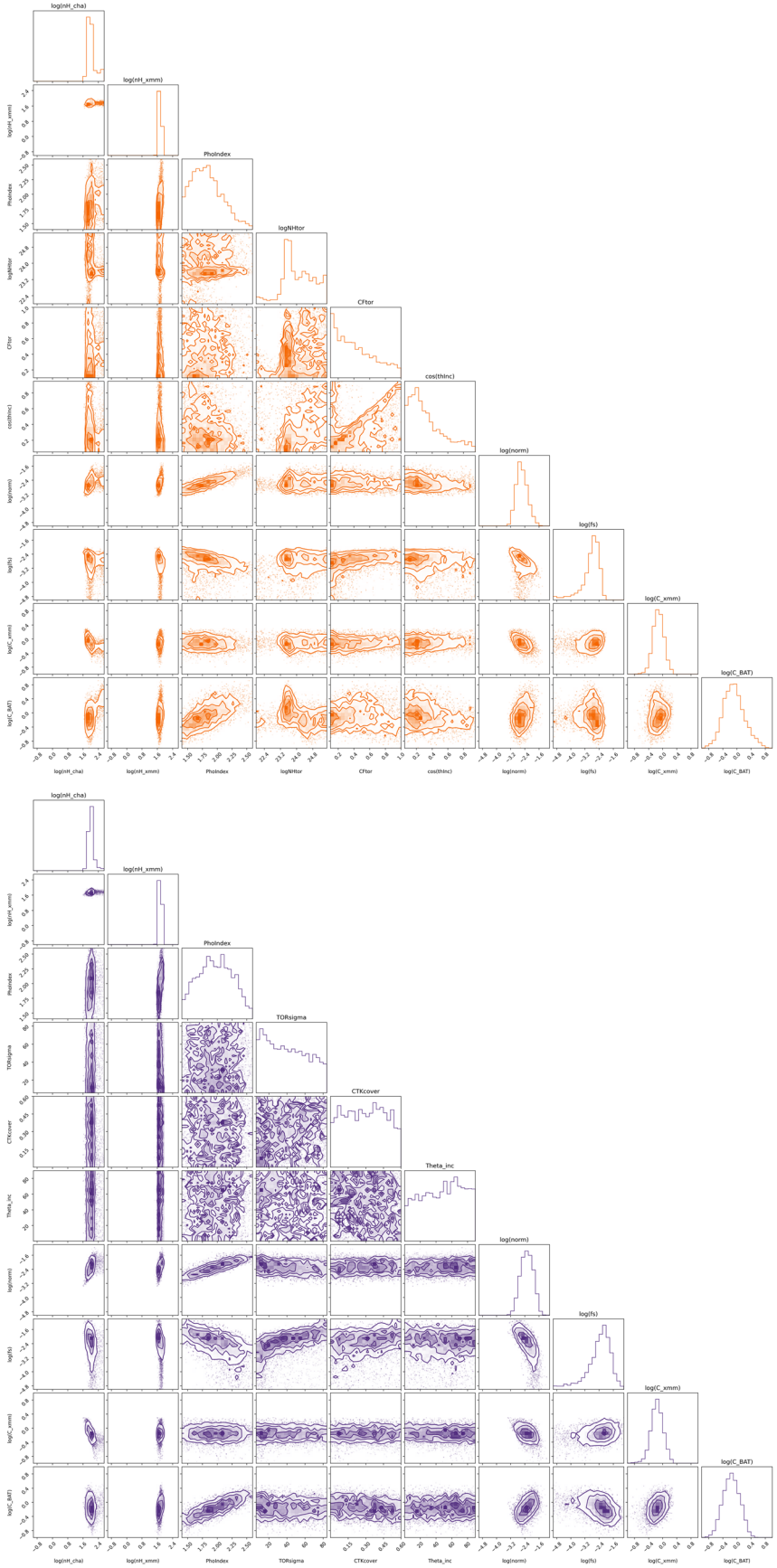

Figure 16. CGCG 1822.3+2053. Top panel: Corner plot for the `borus02` model. Bottom left-hand panel: Corner plot for the `UXCLUMPY` model.

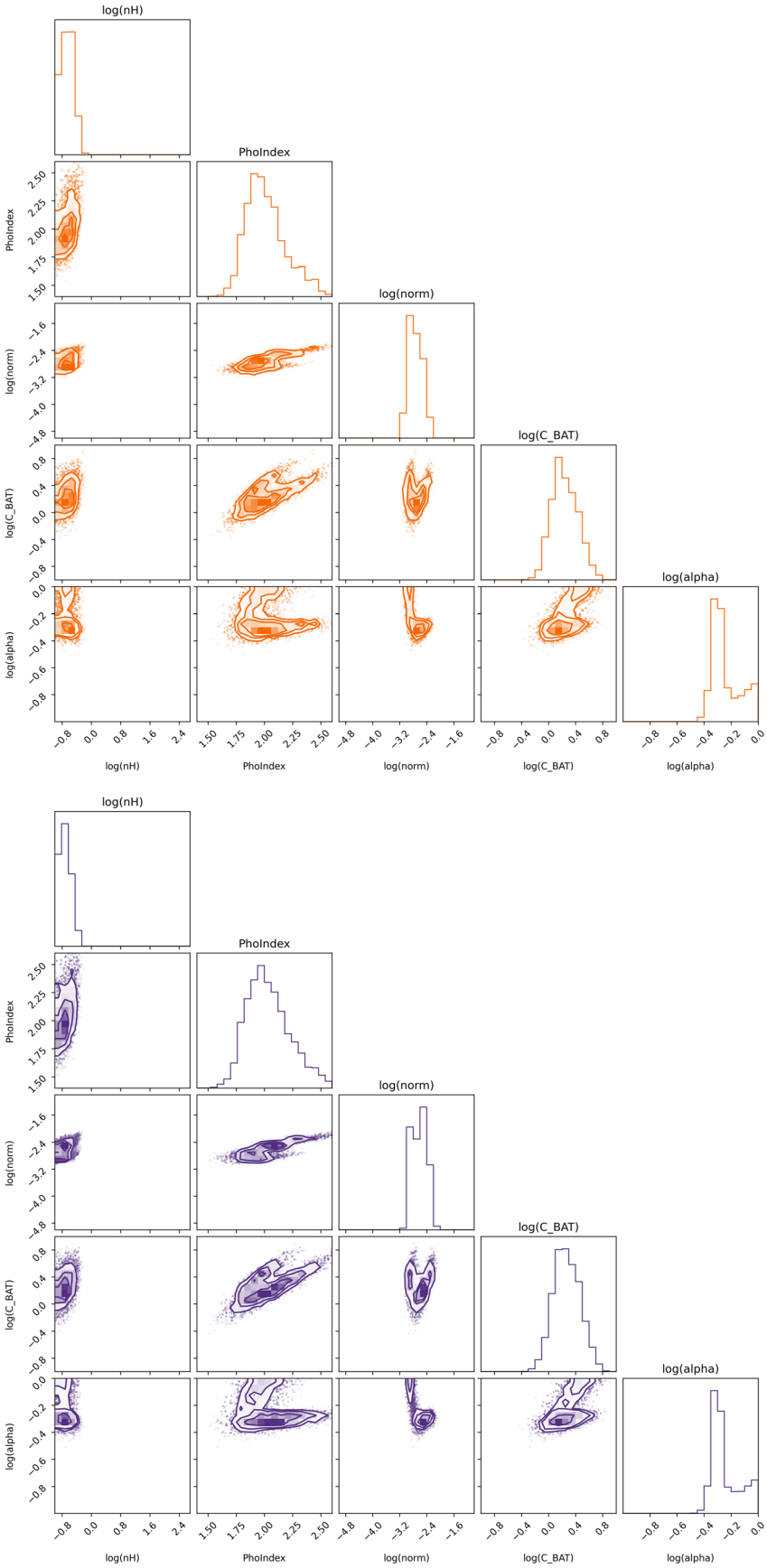

Figure 17. MCG +2-57-2. Top panel: Corner plot for the `borus02` model. Bottom left-hand panel: Corner plot for the `UXCLUMPY` model.

Table 5
2MFGC 9836 Best-fit Results

Model	MYTorus	borus02*	borus02	UXCLUMPY	MYTorus	borus02*	borus02	UXCLUMPY
Algorithm			LM				Nested Sampling	
red χ^2	0.95	1.01	0.95	0.96	0.99	1.01	0.95	0.96
χ^2/d.o.f.	134/141	142/141	131/138	132/138	139/141	142/141	131/138	132/138
Γ	$1.92^{+0.35}_{-0.31}$	$1.99^{+0.20}_{-0.31}$	$1.84^{+0.42}_{-0.19}$	$1.77^{+0.42}_{-0.22}$	$1.91^{+0.35}_{-0.28}$	$1.96^{+0.22}_{-0.29}$	$1.79^{+0.43}_{-0.27}$	$1.89^{+0.43}_{-0.30}$
$N_{\rm H,tor}(10^{22}\ {\rm cm}^{-2})$	$N_{\rm H,ch}$*	100*	3.79^{+u}_{-u}	⋯	$N_{\rm H,ch}$*	100*	$5.27^{+1870}_{-3.87}$	⋯
$\rm CF_{tor}$	⋯	0.67*	0.56^{+u}_{-u}	⋯	⋯	0.67*	$0.16^{+0.78}_{-0.04}$	⋯
$\theta_{\rm inc}(^\circ)$	90*	45*	$81.4^{+u}_{-42.6}$	55.6^{+u}_{-u}	90*	45*	73^{+13}_{-42}	$31.6^{+54.2}_{-25.9}$
$\sigma_{\rm tor}$	⋯	⋯	⋯	$6.99^{+54.62}_{-}$	⋯	⋯	⋯	13.8^{+66}_{-5}
CTKcover	⋯	⋯	⋯	0.25^{+u}_{-u}	⋯	⋯	⋯	$0.44^{+0.13}_{-0.42}$
norm(10^{-3})	$3.30^{+3.10}_{-1.46}$	$3.42^{+1.31}_{-1.55}$	$3.19^{+3.30}_{-1.52}$	$2.77^{+2.30}_{-1.09}$	$3.46^{+2.84}_{-1.55}$	$2.75^{+2.16}_{-0.92}$	$2.98^{+3.25}_{-1.30}$	$4.25^{+5.41}_{-2.05}$
$f_{\rm s}(10^{-3})$	$1.67^{+2.18}_{-1.30}$	$0.01^{+1.18}_{-u}$	$0.01^{+2.78}_{-u}$	⋯	$1.48^{+1.63}_{-1.45}$	$0.04^{+0.69}_{-0.03}$	$0.03^{+2.1}_{-0.02}$	⋯
$f_{\rm s,uxclumpy}(10^{-3})$	⋯	⋯	⋯	1.92^{+u}_{-u}	⋯	⋯	⋯	$2.5^{+9.8}_{-2.5}$
$C_{\rm BAT}$	$0.79^{+0.58}_{-0.33}$	$0.80^{+0.30}_{-0.33}$	$0.75^{+0.42}_{-0.33}$	$0.58^{+0.33}_{-0.22}$	$0.86^{+0.50}_{-0.41}$	$0.72^{+0.36}_{-0.27}$	$0.65^{+0.62}_{-0.25}$	$0.61^{+0.58}_{-0.26}$
$N_{\rm H,ch}(10^{22}\ {\rm cm}^{-2})$	$17.2^{+2.5}_{-2.3}$	$17.4^{+1.6}_{-2.7}$	$18.3^{+2.5}_{-3.0}$	$14.4^{+3.7}_{-1.5}$	$16.9^{+2.7}_{-2.0}$	$16.8^{+2.8}_{-2.0}$	$17.3^{+3.9}_{-2.1}$	$15.9^{+2.7}_{-2.5}$
$\log(L_{\rm 2\text{-}10\,keV,\,cha})$	$43.20^{+0.03}_{-0.03}$	$43.17^{+0.03}_{-0.03}$	$43.23^{+0.03}_{-0.03}$	$43.25^{+0.05}_{-0.05}$	$43.21^{+0.03}_{-0.03}$	$43.17^{+0.03}_{-0.03}$	$43.25^{+0.03}_{-0.03}$	$43.3^{+0.1}_{-0.1}$
$\log(L_{\rm 15\text{-}150\,keV})$	$43.44^{+0.07}_{-0.08}$	$43.26^{+0.09}_{-0.11}$	$43.45^{+0.06}_{-0.07}$	$43.3^{+0.3}_{-0.4}$	$43.45^{+0.07}_{-0.08}$	$43.27^{+0.09}_{-0.11}$	$43.40^{+0.06}_{-0.08}$	$43.4^{+0.3}_{-0.4}$
$\log(F_{\rm 2\text{-}10\,keV,\,cha})$	$-11.45^{+0.03}_{-0.03}$	$-11.45^{+0.03}_{-0.03}$	$-11.44^{+0.03}_{-0.03}$	$-11.43^{+0.03}_{-0.03}$	$-11.45^{+0.03}_{-0.03}$	$-11.45^{+0.03}_{-0.03}$	$-11.44^{+0.03}_{-0.03}$	$-11.43^{+0.03}_{-0.03}$
$\log(F_{\rm 15\text{-}150\,keV})$	$-10.93^{+0.06}_{-0.07}$	$-10.98^{+0.06}_{-0.07}$	$-10.96^{+0.06}_{-0.07}$	$-10.95^{+0.06}_{-0.07}$	$-10.93^{+0.06}_{-0.07}$	$-10.98^{+0.06}_{-0.07}$	$-10.97^{+0.06}_{-0.07}$	$-10.94^{+0.06}_{-0.07}$
$P_{\rm ch}$(CT)	⋯	⋯	⋯	⋯	0.0%	0.0%	0.0%	0.0%

Table 6
NGC 5759 Best-fit Results

Model	MYTorus	borus02*	borus02	UXCLUMPY	MYTorus	borus02*	borus02	UXCLUMPY
Algorithm			LM				Nested Sampling	
red χ^2	1.20	1.13	1.13	1.18	1.11	1.14	1.13	1.21
χ^2/d.o.f.	85/71	80/71	77/68	81/68	79/71	81/71	77/68	82/68
Γ	$1.93^{+0.46}_{-0.47}$	$1.70^{+0.41}_{-u}$	$1.73^{+0.38}_{-0.28}$	$1.72^{+0.45}_{-u}$	$1.85^{+0.41}_{-0.36}$	$1.67^{+0.36}_{-0.22}$	$1.76^{+0.47}_{-0.28}$	$1.71^{+0.54}_{-0.26}$
$N_{\rm H,tor}(10^{22}\ {\rm cm}^{-2})$	100*	100*	65^{+100}_{-u}	⋯	100*	100*	41^{+1800}_{-17}	⋯
$\rm CF_{tor}$	⋯	0.67*	$1.00^{+u}_{-0.54}$	⋯	⋯	0.67*	$0.90^{+0.07}_{-0.68}$	⋯
$\theta_{\rm inc}(^\circ)$	45*	45*	33^{+u}_{-u}	0^{+u}_{-u}	45*	45*	83^{+3}_{-49}	79^{+7}_{-74}
$\sigma_{\rm tor}$	⋯	⋯	⋯	7^{+46}_{-u}	⋯	⋯	⋯	22^{+51}_{-11}
CTKcover	⋯	⋯	⋯	0^{+u}_{-u}	⋯	⋯	⋯	$0.06^{+0.49}_{-0.04}$
norm(10^{-3})	$0.38^{+1.01}_{-u}$	$0.14^{+0.27}_{-u}$	$0.17^{+0.35}_{-0.09}$	13^{+16}_{-10}	$0.78^{+1.49}_{-0.55}$	$0.27^{+0.38}_{-0.17}$	$0.57^{+3.66}_{-0.42}$	$1.65^{+4.79}_{-1.16}$
$f_{\rm s}(10^{-3})$	19^{+31}_{-12}	36^{+49}_{-21}	32^{+22}_{-18}	⋯	9^{+14}_{-6}	24^{+19}_{-14}	14^{+21}_{-12}	⋯
$f_{\rm s,uxclumpy}(10^{-3})$	⋯	⋯	⋯	$0.7^{+u}_{-0.5}$	⋯	⋯	⋯	30^{+43}_{-26}
$C_{\rm xmm}$	$0.92^{+0.98}_{-0.41}$	$1.01^{+1.06}_{-0.45}$	$1.10^{+0.83}_{-0.43}$	$1.01^{+u}_{-0.49}$	$0.66^{+0.66}_{-0.21}$	$0.66^{+0.89}_{-0.21}$	$0.63^{+0.88}_{-0.22}$	$0.62^{+0.64}_{-0.17}$
$C_{\rm BAT}$	$5.73^{+9.86}_{-3.76}$	$5.76^{+8.41}_{-3.41}$	$5.23^{+7.19}_{-3.86}$	$3.39^{+3.51}_{-2.22}$	$2.71^{+4.85}_{-1.33}$	$5.18^{+3.45}_{-2.98}$	$5.38^{+3.78}_{-4.06}$	$1.79^{+2.92}_{-1.08}$
$N_{\rm H,cha}(10^{22}\ {\rm cm}^{-2})$	50^{+63}_{-24}	36^{+44}_{-20}	36^{+42}_{-16}	50^{+75}_{-29}	81^{+350}_{-30}	51^{+390}_{-22}	65^{+390}_{-27}	110^{+340}_{-48}
$N_{\rm H,xmm}(10^{22}\ {\rm cm}^{-2})$	85^{+u}_{-33}	80^{+u}_{-32}	87^{+u}_{-34}	98^{+u}_{-49}	140^{+330}_{-50}	120^{+360}_{-36}	290^{+190}_{-190}	170^{+310}_{-57}
$\log(L_{\rm 2\text{-}10\,keV,\,cha})$	$41.8^{+0.2}_{-0.3}$	$42.0^{+0.2}_{-0.3}$	$42.0^{+0.2}_{-0.2}$	$43.9^{+0.3}_{-0.4}$	$42.3^{+0.2}_{-0.4}$	$41.9^{+0.2}_{-0.3}$	$42.0^{+0.2}_{-0.2}$	$43.1^{+0.3}_{-0.5}$
$\log(L_{\rm 2\text{-}10\,keV,\,xmm})$	$41.8^{+0.2}_{-0.4}$	$42.0^{+0.3}_{-0.8}$	$42.0^{+0.3}_{-0.9}$	$43.9^{+0.3}_{-0.4}$	$42.4^{+0.3}_{-1.7}$	$42.0^{+0.3}_{-0.7}$	$42.1^{+0.3}_{-1.6}$	$43.0^{+0.3}_{-0.5}$
$\log(L_{\rm 15\text{-}150\,keV})$	$42.1^{+0.1}_{-0.1}$	$42.4^{+0.1}_{-0.2}$	$42.4^{+0.1}_{-0.2}$	$44.8^{+0.7}_{-0.6}$	$42.7^{+0.1}_{-0.1}$	$42.4^{+0.1}_{-0.2}$	$42.3^{+0.1}_{-0.2}$	$43.7^{+0.4}_{-0.6}$
$\log(F_{\rm 2\text{-}10\,keV,\,cha})$	$-12.7^{+0.1}_{-0.1}$	$-12.8^{+0.1}_{-0.1}$	$-12.7^{+0.1}_{-0.1}$	$-12.7^{+0.1}_{-0.1}$	$-12.7^{+0.1}_{-0.1}$	$-12.8^{+0.1}_{-0.1}$	$-12.7^{+0.1}_{-0.1}$	$-12.7^{+0.1}_{-0.1}$
$\log(F_{\rm 2\text{-}10\,keV,\,xmm})$	$-13.0^{+0.1}_{-0.1}$	$-13.0^{+0.1}_{-0.1}$	$-13.0^{+0.1}_{-0.1}$	$-13.0^{+0.1}_{-0.1}$	$-13.0^{+0.1}_{-0.1}$	$-13.0^{+0.1}_{-0.1}$	$-13.0^{+0.1}_{-0.1}$	$-13.0^{+0.1}_{-0.1}$
$\log(F_{\rm 15\text{-}150\,keV})$	$-11.0^{+0.1}_{-0.1}$	$-11.0^{+0.1}_{-0.1}$	$-11.0^{+0.1}_{-0.1}$	$-11.0^{+0.1}_{-0.1}$	$-11.0^{+0.1}_{-0.1}$	$-11.0^{+0.1}_{-0.1}$	$-11.0^{+0.1}_{-0.1}$	$-11.0^{+0.1}_{-0.1}$
$P_{\rm ch}$(CT)	⋯	⋯	⋯	⋯	42.6%	38.7%	59.1%	60.6%
$P_{\rm xmm}$(CT)	⋯	⋯	⋯	⋯	80.4%	75.7%	84.1%	86.3%

Table 7
IC 1141 Best-fit Results

Model	MYTorus	borus02*	borus02	UXCLUMPY	MYTorus	borus02*	borus02	UXCLUMPY
Algorithm			LM				Nested Sampling	
red χ^2	1.17	1.06	1.20	1.27	1.28	1.06	1.27	1.27
χ^2/d.o.f.	21/18	19/18	18/15	19/15	23/18	19/18	19/15	19/15
Γ	1.98^{+u}_{-u}	$1.95^{+0.41}_{-u}$	1.96^{+u}_{-u}	$1.83^{+0.71}_{-u}$	$2.03^{+0.46}_{-0.51}$	$1.88^{+0.44}_{-0.36}$	$1.79^{+0.68}_{-0.30}$	$2.35^{+0.19}_{-0.83}$
$N_{\rm H,tor}(10^{22}\ {\rm cm}^{-2})$	${N_{\rm H,ch}}^{*}$	100^{*}	107^{+u}_{-93}	⋯	${N_{\rm H,ch}}^{*}$	100^{*}	28^{+2170}_{-24}	⋯
$\rm CF_{tor}$	⋯	0.67^{*}	0.86^{+u}_{-u}	⋯	⋯	0.67^{*}	$0.26^{+0.65}_{-0.13}$	⋯
$\theta_{\rm inc}(^\circ)$	90^{*}	45^{*}	32^{+u}_{-u}	90^{+u}_{-u}	90^{*}	45^{*}	39^{+44}_{-14}	14^{+62}_{-14}
$\sigma_{\rm tor}$	⋯	⋯	⋯	84^{+u}_{-u}	⋯	⋯	⋯	70^{+10}_{-60}
CTKcover	⋯	⋯	⋯	0.0^{+u}_{-y}	⋯	⋯	⋯	$0.10^{+0.39}_{-0.10}$
norm(10^{-3})	$1.20^{+4.36}_{-u}$	$0.92^{+1.15}_{-0.68}$	$0.94^{+6.72}_{-0.73}$	$1.22^{+4.84}_{-0.93}$	$1.24^{+2.89}_{-0.80}$	$0.86^{+1.03}_{-0.52}$	$1.12^{+4.86}_{-0.78}$	$6.69^{+8.82}_{-6.05}$
$f_{\rm s}(10^{-3})$	$3.68^{+7.65}_{-2.74}$	$0.22^{+9.16}_{-u}$	1.58^{+10}_{-u}	⋯	$3.28^{+5.53}_{-2.36}$	$0.09^{+3.80}_{-0.08}$	$0.58^{+3.8}_{-0.56}$	⋯
$f_{\rm s,uxclumpy}(10^{-3})$	⋯	⋯	⋯	2.4^{+u}_{-u}	⋯	⋯	⋯	9.1^{+30}_{-u}
$C_{\rm BAT}$	$2.01^{+5.06}_{-1.46}$	$2.04^{+3.05}_{-u}$	$1.82^{+2.93}_{-u}$	$1.20^{+u}_{-0.90}$	$2.77^{+2.36}_{-2.12}$	$1.90^{+2.68}_{-1.20}$	$1.29^{+3.39}_{-0.72}$	$0.94^{+1.70}_{-0.71}$
$N_{\rm H,ch}(10^{22}\ {\rm cm}^{-2})$	44^{+15}_{-12}	45^{+16}_{-15}	43^{+69}_{-13}	47^{+23}_{-16}	45^{+14}_{-13}	43^{+22}_{-13}	49^{+120}_{-15}	50^{+92}_{-15}
$\log(L_{\rm 2\text{-}10\,keV,\,cha})$	$42.2^{+0.1}_{-0.1}$	$42.1^{+0.1}_{-0.1}$	$42.1^{+0.1}_{-0.1}$	$42.3^{+0.6}_{-0.4}$	$42.2^{+0.1}_{-0.1}$	$42.1^{+0.1}_{-0.1}$	$42.2^{+0.1}_{-0.1}$	$42.7^{+0.4}_{-0.6}$
$\log(L_{\rm 15\text{-}150\,keV})$	$42.4^{+0.1}_{-0.1}$	$42.2^{+0.2}_{-0.3}$	$42.2^{+0.1}_{-0.3}$	$42.6^{+0.6}_{-0.4}$	$42.3^{+0.1}_{-0.2}$	$42.2^{+0.2}_{-0.3}$	$42.2^{+0.2}_{-0.3}$	$42.7^{+0.5}_{-0.6}$
$\log(F_{\rm 2\text{-}10\,keV,\,cha})$	$-12.27^{+0.08}_{-0.08}$	$-12.29^{+0.08}_{-0.08}$	$-12.28^{+0.08}_{-0.08}$	$-12.24^{+0.08}_{-0.08}$	$-12.28^{+0.08}_{-0.08}$	$-12.29^{+0.08}_{-0.08}$	$-12.29^{+0.08}_{-0.08}$	$-12.25^{+0.08}_{-0.08}$
$\log(F_{\rm 15\text{-}150\,keV})$	$-11.1^{+0.1}_{-0.2}$	$-11.1^{+0.1}_{-0.2}$	$-11.1^{+0.1}_{-0.1}$	$-11.1^{+0.1}_{-0.1}$	$-11.1^{+0.1}_{-0.2}$	$-11.1^{+0.1}_{-0.2}$	$-11.2^{+0.1}_{-0.2}$	$-11.1^{+0.1}_{-0.1}$
$P_{\rm ch}$(CT)	⋯	⋯	⋯	⋯	0.0%	0.1%	5.5%	4.4%

Table 8
2MASX J17253053–4510279 Best-fit Results

Model	Simple	borus02	UXCLUMPY	Simple	borus02	UXCLUMPY
Algorithm		LM			Nested Sampling	
red χ^2	0.80	0.93	0.92	0.93	0.93	0.93
χ^2/d.o.f.	252/314	291/313	289/313	292/314	292/313	292/313
Γ	$1.76^{+0.15}_{-0.09}$	$1.79^{+0.11}_{-0.12}$	$1.70^{+0.13}_{-0.06}$	$1.78^{+0.10}_{-0.08}$	$1.85^{+0.10}_{-0.08}$	$1.83^{+0.10}_{-0.08}$
$N_{\rm H,tor}(10^{22}\ {\rm cm}^{-2})$	⋯	100^{*}	⋯	⋯	100^{*}	⋯
$\rm CF_{tor}$	⋯	0.67^{*}	⋯	⋯	0.67^{*}	⋯
$\theta_{\rm inc}(^\circ)$	90^{*}	45^{*}	90^{*}	90^{*}	45^{*}	90^{*}
$\sigma_{\rm tor}$	⋯	⋯	28^{*}	⋯	⋯	28^{*}
CTKcover	⋯	⋯	0^{*}	⋯	⋯	0^{*}
norm(10^{-3})	$0.26^{+0.06}_{-0.05}$	$0.32^{+0.06}_{-0.05}$	$0.38^{+0.08}_{-0.09}$	$0.33^{+0.05}_{-0.04}$	$0.35^{+0.06}_{-0.05}$	$0.44^{+0.07}_{-0.09}$
$C_{\rm xmm}$	$2.16^{+0.27}_{-0.23}$	$1.95^{+0.22}_{-0.20}$	$1.92^{+0.31}_{-0.21}$	$1.99^{+0.23}_{-0.18}$	$1.96^{+0.24}_{-0.19}$	$1.86^{+0.41}_{-0.18}$
$C_{\rm BAT}$	$5.74^{+3.02}_{-1.54}$	$3.78^{+1.45}_{-1.29}$	$3.13^{+1.62}_{-0.96}$	$4.83^{+1.63}_{-1.33}$	$4.30^{+1.42}_{-1.24}$	$4.21^{+1.49}_{-1.13}$
$N_{\rm H,cha}(10^{22}\ {\rm cm}^{-2})$	$0.38^{+0.21}_{-0.18}$	$0.50^{+0.18}_{-0.20}$	$0.51^{+0.17}_{-0.16}$	$0.53^{+0.17}_{-0.17}$	$0.54^{+0.21}_{-0.15}$	$0.46^{+0.16}_{-0.14}$
$N_{\rm H,xmm}(10^{22}\ {\rm cm}^{-2})$	$0.02^{+0.13}_{-u}$	$0.07^{+0.11}_{-u}$	$0.16^{+0.11}_{-u}$	$0.11^{+0.09}_{-0.01}$	$0.12^{+0.12}_{-0.02}$	$0.11^{+0.08}_{-0.01}$
$\log(L_{\rm 2\text{-}10\,keV,\,cha})$	$41.87^{+0.03}_{-0.03}$	$41.95^{+0.03}_{-0.03}$	$42.42^{+0.05}_{-0.08}$	$41.96^{+0.03}_{-0.03}$	$41.95^{+0.03}_{-0.03}$	$42.39^{+0.05}_{-0.06}$
$\log(L_{\rm 2\text{-}10\,keV,\,xmm})$	$41.87^{+0.02}_{-0.02}$	$41.95^{+0.02}_{-0.02}$	$42.71^{+0.05}_{-0.08}$	$41.96^{+0.02}_{-0.02}$	$41.94^{+0.02}_{-0.02}$	$42.68^{+0.05}_{-0.06}$
$\log(L_{\rm 15\text{-}150\,keV})$	$42.2^{+0.1}_{-0.1}$	$42.2^{+0.1}_{-0.1}$	$43.3^{+0.2}_{-0.2}$	$42.3^{+0.1}_{-0.1}$	$42.2^{+0.1}_{-0.1}$	$43.3^{+0.1}_{-0.1}$
$\log(F_{\rm 2\text{-}10\,keV,\,cha})$	$-12.06^{+0.03}_{-0.03}$	$-11.96^{+0.03}_{-0.03}$	$-11.96^{+0.03}_{-0.03}$	$-11.97^{+0.03}_{-0.03}$	$-11.96^{+0.03}_{-0.03}$	$-11.98^{+0.03}_{-0.03}$
$\log(F_{\rm 2\text{-}10\,keV,\,xmm})$	$-11.71^{+0.02}_{-0.02}$	$-11.65^{+0.02}_{-0.02}$	$-11.65^{+0.02}_{-0.02}$	$-11.66^{+0.02}_{-0.02}$	$-11.65^{+0.02}_{-0.02}$	$-11.66^{+0.02}_{-0.02}$
$\log(F_{\rm 15\text{-}150\,keV})$	$-10.96^{+0.08}_{-0.10}$	$-10.95^{+0.08}_{-0.10}$	$-10.95^{+0.08}_{-0.10}$	$-10.96^{+0.08}_{-0.10}$	$-10.97^{+0.08}_{-0.10}$	$-10.97^{+0.08}_{-0.10}$
$P_{\rm ch}$(CT)	⋯	⋯	⋯	0.0%	0.0%	0.0%
$P_{\rm xmm}$(CT)	⋯	⋯	⋯	0.0%	0.0%	0.0%

Table 9
MCG +2-57-2 Best-fit Results

Model Algorithm	Simple	borus02 LM	UXCLUMPY	Simple	borus02 Nested Sampling	UXCLUMPY
red χ^2	0.97	1.01	1.01	1.01	1.01	1.01
χ^2/d.o.f.	199/205	207/205	208/205	208/205	207/205	208/205
α	$1^{+}_{-0.23}$	$1^{+}_{-0.5}$	$1^{+}_{-0.5}$	$0.5^{+0.4}_{-0.1}$	$0.5^{+0.4}_{-0.1}$	$0.5^{+0.4}_{-0.1}$
Γ	$1.90^{+0.24}_{-0.23}$	$2.00^{+0.07}_{-0.27}$	$1.99^{+0.13}_{-0.24}$	$1.99^{+0.43}_{-0.24}$	$1.93^{+0.43}_{-0.16}$	$1.97^{+0.43}_{-0.20}$
$N_{\rm H,tor}(10^{22}\ {\rm cm}^{-2})$	⋯	100^{*}	⋯	⋯	100^{*}	⋯
$\rm CF_{tor}$	⋯	0.67^{*}	⋯	⋯	0.67^{*}	⋯
$\theta_{\rm inc}(^\circ)$	90^{*}	45^{*}	90^{*}	90^{*}	45^{*}	90^{*}
$\sigma_{\rm tor}$	⋯	⋯	28^{*}	⋯	⋯	28^{*}
CTKcover	⋯	⋯	0^{*}	⋯	⋯	0^{*}
norm(10^{-3})	$0.72^{+0.27}_{-0.18}$	$0.99^{+3.38}_{-0.17}$	$1.20^{+3.90}_{-0.14}$	$2.77^{+1.45}_{-1.83}$	$1.14^{+2.93}_{-0.17}$	$1.39^{+3.75}_{-0.20}$
$C_{\rm BAT}$	$3.99^{+3.27}_{-1.89}$	$3.24^{+0.92}_{-2.49}$	$3.37^{+2.30}_{-2.59}$	$2.05^{+3.13}_{-0.94}$	$1.44^{+2.26}_{-0.56}$	$1.56^{+2.43}_{-0.65}$
$N_{\rm H,ch}(10^{22}\ {\rm cm}^{-2})$	$0.17^{+0.26}_{-u}$	$0.17^{+0.20}_{-u}$	$0.14^{+0.17}_{-u}$	$0.19^{+0.23}_{-0.07}$	$0.16^{+0.26}_{-0.05}$	$0.14^{+0.22}_{-0.03}$
$\log(L_{\rm 2\text{-}10\,keV,\,cha})$	$42.62^{+0.03}_{-0.03}$	$42.67^{+0.03}_{-0.03}$	$42.8^{+0.4}_{-0.1}$	$42.53^{+0.02}_{-0.02}$	$42.67^{+0.03}_{-0.03}$	$43.2^{+0.1}_{-0.3}$
$\log(L_{\rm 15\text{-}150\,keV})$	$42.8^{+0.1}_{-0.1}$	$42.8^{+0.1}_{-0.1}$	$43.4^{+0.6}_{-0.3}$	$42.5^{+0.1}_{-0.1}$	$42.7^{+0.1}_{-0.1}$	$43.1^{+0.5}_{-0.2}$
$\log(F_{\rm 2\text{-}10\,keV,\,cha})$	$-11.69^{+0.03}_{-0.03}$	$-11.61^{+0.03}_{-0.03}$	$-11.62^{+0.03}_{-0.03}$	$-11.67^{+0.03}_{-0.03}$	$-11.61^{+0.03}_{-0.03}$	$-11.63^{+0.03}_{-0.03}$
$\log(F_{\rm 15\text{-}150\,keV})$	$-10.89^{+0.07}_{-0.08}$	$-10.91^{+0.07}_{-0.08}$	$-10.91^{+0.07}_{-0.08}$	$-10.91^{+0.07}_{-0.08}$	$-10.91^{+0.07}_{-0.08}$	$-10.91^{+0.07}_{-0.08}$
$P_{\rm ch}$(CT)	⋯	⋯	⋯	0.0%	0.0%	0.0%

ORCID iDs

Isaiah S. Cox https://orcid.org/0000-0003-2287-0325
Núria Torres-Albà https://orcid.org/0000-0003-3638-8943
Stefano Marchesi https://orcid.org/0000-0001-5544-0749
Peter Boorman https://orcid.org/0000-0001-9379-4716
Xiurui Zhao https://orcid.org/0000-0002-7791-3671
Ross Silver https://orcid.org/0000-0001-6564-0517
Marco Ajello https://orcid.org/0000-0002-6584-1703
Indrani Pal https://orcid.org/0000-0002-7825-1526

References

Ajello, M., Greiner, J., Sato, G., et al. 2008, ApJ, 689, 666
Ajello, M., Rau, A., Greiner, J., et al. 2008, ApJ, 673, 96
Alexander, D. M., Bauer, F. E., Brandt, W. N., et al. 2003, AJ, 126, 539
Ananna, T. T., Treister, E., Urry, C. M., et al. 2019, ApJ, 871, 240
Antonucci, R. 1993, ARA&A, 31, 473
Arévalo, P., Bauer, F. E., Puccetti, S., et al. 2014, ApJ, 791, 81
Balokovic, M., Brightman, M., Harrison, F. A., et al. 2018, ApJ, 854, 42
Baloković, M., Harrison, F. A., Madejski, G., et al. 2020, ApJ, 905, 41
Barthelmy, S. D., Barbier, L. M., Cummings, J. R., et al. 2005, SSRv, 120, 143
Bauer, F. E., Arévalo, P., Walton, D. J., et al. 2015, ApJ, 812, 116
Bonamente, M. 2020, JApSt, 47, 2044
Boorman, P. G., Torres-Albà, N., Annuar, A., et al. 2024, FrASS, 11, 1335459
Brightman, M., Baloković, M., Stern, D., et al. 2015, ApJ, 805, 41
Buchner, J. 2021, JOSS, 6, 3001
Buchner, J. 2022, RNAAS, 6, 89
Buchner, J. 2023, Statistics Surveys, 17
Buchner, J., & Boorman, P. 2024, in Handbook of X-ray and Gamma-ray Astrophysics, ed. C. Bambi & A. Santangelo (Singapore: Springer), 5403
Buchner, J., Brightman, M., Nandra, K., Nikutta, R., & Bauer, F. E. 2019, A&A, 629, A16
Buchner, J., Georgakakis, A., Nandra, K., et al. 2014, A&A, 564, A125
Burlon, D., Ajello, M., Greiner, J., et al. 2011, ApJ, 728, 58
Cappelluti, N., Li, Y., Ricarte, A., et al. 2017, ApJ, 837, 19
Chen, Y.-P., Zaw, I., Farrar, G. R., & Elgamal, S. 2022, ApJS, 258, 29
Comastri, A., Setti, G., Zamorani, G., & Hasinger, G. 1995, A&A, 296, 1
Cox, I. 2024, Relative Entropy, v1.0.2, Zenodo, doi:10.5281/zenodo.14225570
Davis, J. E. 2001, ApJ, 562, 575
Della Ceca, R., Caccianiga, A., Severgnini, P., et al. 2008, A&A, 487, 119
European Space Agency 2023, Compton-thick AGN: The Hunt Continues, 19.17_20220121_1250, European Space Agency, doi:10.57780/esa-96gy8kq
Fruscione, A., McDowell, J. C., Allen, G. E., et al. 2006, Proc. SPIE, 6270, 62701V
Gandhi, P., & Fabian, A. C. 2003, MNRAS, 339, 1095
Garcet, O., Gandhi, P., Gosset, E., et al. 2007, A&A, 474, 473
Ghisellini, G., Haardt, F., & Matt, G. 1994, MNRAS, 267, 743
Gilli, R., Comastri, A., & Hasinger, G. 2007, A&A, 463, 79
Gilli, R., Risaliti, G., & Salvati, M. 1999, A&A, 347, 424
Gordon, C., & Arnaud, K., 2021 PyXspec: Python Interface to XSPEC Spectral-fitting Program, Astrophysics Source Code Library, ascl:2101.014
Haardt, F., & Maraschi, L. 1993, ApJ, 413, 507
Harrison, F. A., Aird, J., Civano, F., et al. 2016, ApJ, 831, 185
Hickox, R. C., & Markevitch, M. 2006, ApJ, 645, 95
Jansen, F., Lumb, D., Altieri, B., et al. 2001, A&A, 365, L1
Kallová, K., Boorman, P. G., & Ricci, C. 2024, ApJ, 966, 116
Koss, M., Trakhtenbrot, B., Ricci, C., et al. 2017, ApJ, 850, 74
Koss, M. J., Assef, R., Balokovic, M., et al. 2016, ApJ, 825, 85
Koss, M. J., Trakhtenbrot, B., Ricci, C., et al. 2022, ApJS, 261, 6
Kullback, S., & Leibler, R. A. 1951, The Annals of Mathematical Statistics, 22, 79
Lanzuisi, G., Civano, F., Marchesi, S., et al. 2018, MNRAS, 480, 2578
Malizia, A., Bassani, L., Landi, R., et al. 2023, A&A, 671, A152
Marchesi, S., Ajello, M., Comastri, A., et al. 2017a, ApJ, 836, 116
Marchesi, S., Ajello, M., Marcotulli, L., et al. 2018, ApJ, 854, 49
Marchesi, S., Ajello, M., Zhao, X., et al. 2019, ApJ, 872, 8
Marchesi, S., Lanzuisi, G., Civano, F., et al. 2016, ApJ, 830, 100
Marchesi, S., Tremblay, L., Ajello, M., et al. 2017b, ApJ, 848, 53
Matt, G., & Fabian, A. C. 1994, MNRAS, 267, 187
Merloni, A., Bongiorno, A., Brusa, M., et al. 2014, MNRAS, 437, 3550
Miniutti, G., Sanfrutos, M., Beuchert, T., et al. 2014, MNRAS, 437, 1776
Murphy, K. D., & Yaqoob, T. 2009, MNRAS, 397, 1549
Nandra, K., & Pounds, K. A. 1994, MNRAS, 268, 405
Oh, K., Koss, M., Markwardt, C. B., et al. 2018, ApJS, 235, 4
Pizzetti, A., Torres-Alba, N., Marchesi, S., et al. 2022, ApJ, 936, 149
Pizzetti, A., Torres-Alb, N., Marchesi, S., et al. 2025, ApJ, submitted
Reeves, J. N., & Turner, M. J. L. 2000, MNRAS, 316, 234
Ricci, C., Ueda, Y., Koss, M. J., et al. 2015, ApJL, 815, L13
Ricci, F., Treister, E., Bauer, F. E., et al. 2022, ApJS, 261, 8
Risaliti, G., Elvis, M., Fabbiano, G., et al. 2007, ApJL, 659, L111
Risaliti, G., Marconi, A., Maiolino, R., Salvati, M., & Severgnini, P. 2001, A&A, 371, 37
Saha, T., Markowitz, A. G., & Buchner, J. 2022, MNRAS, 509, 5485

Scott, D. W. 2015, Multivariate Density Estimation: Theory, Practice, and Visualization (New York: Wiley)
Segreto, A., Cusumano, G., Ferrigno, C., et al. 2010, A&A, 510, A47
Sengupta, D., Marchesi, S., Vignali, C., et al. 2023, A&A, 676, A103
Serafinelli, R., Braito, V., Reeves, J. N., et al. 2023, A&A, 672, A10
Shimizu, T. T., Davies, R. I., Koss, M., et al. 2018, ApJ, 856, 154
Silver, R., Torres-Albà, N., Zhao, X., et al. 2022a, ApJ, 932, 43
Silver, R., Torres-Albà, N., Zhao, X., et al. 2022b, ApJ, 940, 148
Smith, K. L., Mushotzky, R. F., Koss, M., et al. 2020, MNRAS, 492, 4216
Toba, Y., Oyabu, S., Matsuhara, H., et al. 2014, ApJ, 788, 45
Torres-Albà, N., Marchesi, S., Zhao, X., et al. 2023, A&A, 678, A154
Torres-Albà, N., Marchesi, S., Zhao, X., et al. 2021, ApJ, 922, 252
Traina, A., Marchesi, S., Vignali, C., et al. 2021, ApJ, 922, 159
Treister, E., Urry, C. M., & Virani, S. 2009, ApJ, 696, 110
Ueda, Y., Akiyama, M., Hasinger, G., Miyaji, T., & Watson, M. G. 2014, ApJ, 786, 104
Urry, C. M., & Padovani, P. 1995, PASP, 107, 803
Vasudevan, R. V., Brandt, W. N., Mushotzky, R. F., et al. 2013, ApJ, 763, 111
Virtanen, P., Gommers, R., Oliphant, T. E., et al. 2020, NatMe, 17, 261
Voges, W., Aschenbach, B., Boller, T., et al. 1999, A&A, 349, 389
Wachter, K., Leach, R., & Kellogg, E. 1979, ApJ, 230, 274
Worsley, M. A., Fabian, A. C., Bauer, F. E., et al. 2005, MNRAS, 357, 1281
Zhao, X., Marchesi, S., & Ajello, M. 2019a, ApJ, 871, 182
Zhao, X., Marchesi, S., Ajello, M., et al. 2021, A&A, 650, A57
Zhao, X., Marchesi, S., Ajello, M., et al. 2019b, ApJ, 870, 60